

THE EFFECT OF ANISOTROPIC VISCOSITY ON COLD FRONTS IN GALAXY CLUSTERS

J. A. ZUHONE^{1,2}, M. W. KUNZ³, M. MARKEVITCH¹, J. M. STONE³, V. BIFFI⁴*Draft version December 3, 2024*

ABSTRACT

Cold fronts – contact discontinuities in the intracluster medium (ICM) of galaxy clusters – should be disrupted by Kelvin-Helmholtz (K-H) instabilities due to the associated shear velocity. However, many observed cold fronts appear stable. This opens the possibility to place constraints on microphysical mechanisms that stabilize them, such as the ICM viscosity and/or magnetic fields. We performed exploratory high-resolution simulations of cold fronts arising from subsonic gas sloshing in cluster cores using the grid-based *Athena* MHD code, comparing the effects of isotropic Spitzer and anisotropic Braginskii viscosity (expected in a magnetized plasma). Magnetized simulations with full Braginskii viscosity or isotropic Spitzer viscosity reduced by a factor $f \sim 0.1$ are both in qualitative agreement with observations in terms of suppressing K-H instabilities. The RMS velocity of turbulence within the sloshing region is only modestly reduced by Braginskii viscosity. We also performed unmagnetized simulations with and without viscosity and find that magnetic fields have a substantial effect on the appearance of the cold fronts, even if the initial field is weak and the viscosity is the same. This suggests that determining the dominant suppression mechanism of a given cold front from X-ray observations (e.g. viscosity or magnetic fields) by comparison with simulations is not straightforward. Finally, we performed simulations including anisotropic thermal conduction, and find that including Braginskii viscosity in these simulations does not significantly affect the evolution of cold fronts; they are rapidly smeared out by thermal conduction, as in the inviscid case.

Subject headings: conduction — galaxies: clusters: general — X-rays: galaxies: clusters — methods: hydrodynamic simulations

1. INTRODUCTION

X-ray observations of the intracluster medium (ICM) of galaxy clusters often show sharp surface brightness discontinuities. Spectral analysis of these regions have revealed that in most cases the brighter (and therefore denser) side of the edge is the colder side, and hence these jumps in gas density have been dubbed “cold fronts” (for a detailed review see Markevitch & Vikhlinin 2007). Cluster cold fronts are generally classified into two classes. The first are those which occur in clusters undergoing major mergers, such as 1E 0657-558 (the “Bullet Cluster” Markevitch et al. 2002), A3667 (Vikhlinin et al. 2001a,b; Vikhlinin & Markevitch 2002), and also the elliptical galaxy NGC 1404 (Machacek et al. 2005). In those cases, the cold front is formed by the action of ram pressure on a cluster core moving at high velocity through another cluster’s ICM (cf. Figure 23 of Markevitch & Vikhlinin 2007). The second class of cold fronts occur in “cool-core” systems, exhibited as edges in X-ray surface brightness approximately concentric with respect to the brightness peak of the cluster (e.g., Mazzotta et al. 2001; Markevitch et al. 2001, 2003); these are observed in a majority of cool-core systems (Ghizzardi et al. 2010). Prominent examples include A2142 (Markevitch et al. 2000), A1644

(Srinivasan & Mohr 2001; Johnson et al. 2010), and A1795 (Markevitch et al. 2001). These primarily spiral-shaped cold fronts are believed to arise from gas sloshing in the deep dark-matter-dominated potential well. These motions are initiated when the low-entropy, cool gas of the core is displaced from the bottom of the potential well, either by gravitational perturbations from infalling subclusters (Ascasibar & Markevitch 2006) or by an interaction with a shock front (Churazov et al. 2003).

Most (but not all, see Roediger et al. 2012, for an example) observed cold fronts have smooth, arc-like shapes. As cold fronts move through the surrounding ICM, significant (but subsonic) shear flows develop. These flows can develop Kelvin-Helmholtz (K-H) instabilities. This is certainly the case if the ICM were an inviscid, unmagnetized plasma, as was demonstrated by Zuhone et al. (e.g. 2010, hereafter ZMJ10) and Roediger & Zuhone (2012).

However, Faraday rotation measurements and radio observations of clusters indicate that the ICM is magnetized (see Carilli & Taylor 2002; Ferrari et al. 2008, for recent reviews). Magnetic fields, oriented parallel to a shearing surface and contributing a pressure comparable to the kinetic energy per unit volume of the shear flow, will suppress the growth of the K-H instability (Landau & Lifshitz 1960; Chandrasekhar 1961). For a cold front in the galaxy cluster A3667, Vikhlinin et al. (2001a) and Vikhlinin & Markevitch (2002) determined that the magnetic-field strength required to stabilize the front is $B \sim 10 \mu\text{G}$, roughly an order of magnitude higher than the field strengths usually inferred from radio observations and rotation measure estimates. However, Lyutikov (2006) pointed out that the shear flows around cold fronts lead to “magnetic draping.” Provided the motion of the front is super-Alfvénic, a weak,

¹ Astrophysics Science Division, Laboratory for High Energy Astrophysics, Code 662, NASA/Goddard Space Flight Center, Greenbelt, MD 20771

² Department of Astronomy, University of Maryland, College Park, MD, 20742-2421, USA

³ Department of Astrophysical Sciences, 4 Ivy Lane, Peyton Hall, Princeton University, Princeton, NJ 08544, U. S. A.

⁴ SISSA - Scuola Internazionale Superiore di Studi Avanzati, Via Bonomea 265, 34136 Trieste, Italy

tangled magnetic field will be stretched by this shear flow to produce a layer parallel to the front surface. The energy of the magnetic field in this layer would be increased due to shear amplification, possibly becoming strong enough to stabilize the front against K-H instabilities (Keshet et al. 2010). A number of numerical simulations (e.g. Asai et al. 2004, 2007; Dursi 2007; Dursi & Pfrommer 2008) have demonstrated this stabilizing effect in simplified situations.

The inviscid MHD simulations presented in ZuHone et al. (2011, hereafter ZML11) showed that gas sloshing in cool cores produces relatively strong magnetic fields by shear amplification along the cold front surfaces, resulting in draping layers that suppress K-H instabilities along the fronts. The suppression depended on the assumed strength of the initial field; for a range of field strengths close to those observed in cluster cores, the suppression was only partial, indicating that in general the magnetic field cannot always be relied upon to stabilize cold fronts. In these cases, K-H instabilities not only disrupt the cold fronts but also the magnetic draping layers, re-tangling the field lines. Similar simulations including anisotropic thermal conduction were performed by ZuHone et al. (2013). These demonstrated that the tangling of field lines along the draping layers as well as hot gas that is unshielded from the cold gas of the front results in a significant flow of heat to the cold front, smearing the fronts out to the extent that they would be unobservable in X-rays.

Viscosity may also play a role in stabilizing cold fronts against K-H instabilities. Recently, Roediger et al. (2013a) investigated the effects of isotropic viscosity on cold fronts in a hydrodynamic simulation of the Virgo cluster. Those authors showed that suppression of these instabilities at a level consistent with observational constraints could be obtained by assuming an isotropic Spitzer viscosity with a suppression factor $f = 0.1$. One limitation in this approach is that it neglects the effects of the magnetic field in the ICM. Typical conditions prevailing in the ICM indicate that the mean free path is $\sim 10^{11} - 10^{13}$ times larger than the Larmor radius $r_{g,i}$ (Schekochihin & Cowley 2006), so that the transport of momentum is strongly anisotropic. The consequent restriction of viscous dissipation to the motions and gradients parallel to the magnetic field is known as the ‘‘Braginskii’’ viscosity (Braginskii 1965). For an isotropically tangled magnetic field, the effective viscosity on large scales is $1/5$ the Spitzer value, so that in some situations it may be possible to model the viscous flux as isotropic with a suppression factor. However, as mentioned above, the magnetic-field lines at the cold front are likely to be (mostly) draped parallel to the front by shear amplification, preventing viscous damping of the velocity shear perpendicular to the front surface. Along these lines, Suzuki et al. (2013) recently simulated the propagation of a cold, dense mass of gas in an idealized magnetized ICM with isotropic and anisotropic viscosity. They showed that anisotropic viscosity is far less effective than isotropic viscosity at suppressing K-H instabilities at the cold front that develops. However, their study was limited since it involved a simplified setup, including an initially uniform magnetic field geometry.

In this work, we build upon earlier work by ZMJ10, ZML11, and Z13 to include the effects of viscosity in

simulations of gas sloshing in cool-core galaxy clusters. We try various forms and strengths of the viscosity, and construct synthetic X-ray observations in order to see if the effects can be detectable in X-ray images of real clusters. We show that Braginskii viscosity, in combination with magnetic fields, may provide an explanation for the observed smoothness of cold fronts in sloshing cool cores without completely suppressing K-H instabilities. We also find that an isotropic Spitzer viscosity with $f = 0.1$, in combination with magnetic fields, produces smooth cold fronts and turbulence similar to the Braginskii case. However, using unmagnetized simulations for comparison, we also show that even if the ICM is viscous, the presence or the absence of the magnetic field can still have a substantial effect on the appearance of the cold fronts, complicating the use of these simulations to discern the dominant mechanism for suppression of K-H instabilities. Finally, we show that the additional stability imparted to cold fronts and their magnetic draping layers by viscosity does not prevent anisotropic thermal conduction (at its full Spitzer strength) from smoothing out the sharp cold front jumps, thus rendering them unobservable.

This paper is organized as follows. In Section 2 we describe the simulations and the code. In Section 3 we describe the effects of anisotropic viscosity. Finally, in Section 4 we summarize our results and discuss future developments of this work. Throughout, we assume a flat Λ CDM cosmology with $h = 0.71$ and $\Omega_m = 0.27$.

2. METHOD OF SOLUTION

2.1. Equations

Our simulations solve the following set of MHD equations:

$$\frac{\partial \rho}{\partial t} + \nabla \cdot (\rho \mathbf{v}) = 0, \quad (1)$$

$$\frac{\partial(\rho \mathbf{v})}{\partial t} + \nabla \cdot \left(\rho \mathbf{v} \mathbf{v} - \frac{\mathbf{B} \mathbf{B}}{4\pi} + p \mathbf{I} \right) = \rho \mathbf{g} - \nabla \cdot \Pi, \quad (2)$$

$$\frac{\partial E}{\partial t} + \nabla \cdot \left[\mathbf{v}(E + p) - \frac{\mathbf{B}(\mathbf{v} \cdot \mathbf{B})}{4\pi} \right] = \rho \mathbf{g} \cdot \mathbf{v} - \nabla \cdot \mathbf{Q} - \nabla \cdot (\Pi \cdot \mathbf{v}), \quad (3)$$

$$\frac{\partial \mathbf{B}}{\partial t} + \nabla \cdot (\mathbf{v} \mathbf{B} - \mathbf{B} \mathbf{v}) = 0, \quad (4)$$

where

$$p = p_{\text{th}} + \frac{B^2}{8\pi} \quad (5)$$

is the total pressure,

$$E = \frac{\rho v^2}{2} + \epsilon + \frac{B^2}{8\pi} \quad (6)$$

is the total energy per unit volume, ρ is the gas density, \mathbf{v} is the fluid velocity, p_{th} is the gas pressure, ϵ is the gas internal energy per unit volume, \mathbf{B} is the magnetic field vector, and \mathbf{I} is the unit dyad. We assume an ideal equation of state with $\gamma = 5/3$, equal electron and ion temperatures, and primordial abundances with molecular weight $\bar{A} = 0.6$.

We model the viscous transport of momentum as either isotropic or anisotropic. The viscous flux in the isotropic case is given by

$$\Pi_{\text{iso}} = -\mu \nabla \mathbf{v}, \quad (7)$$

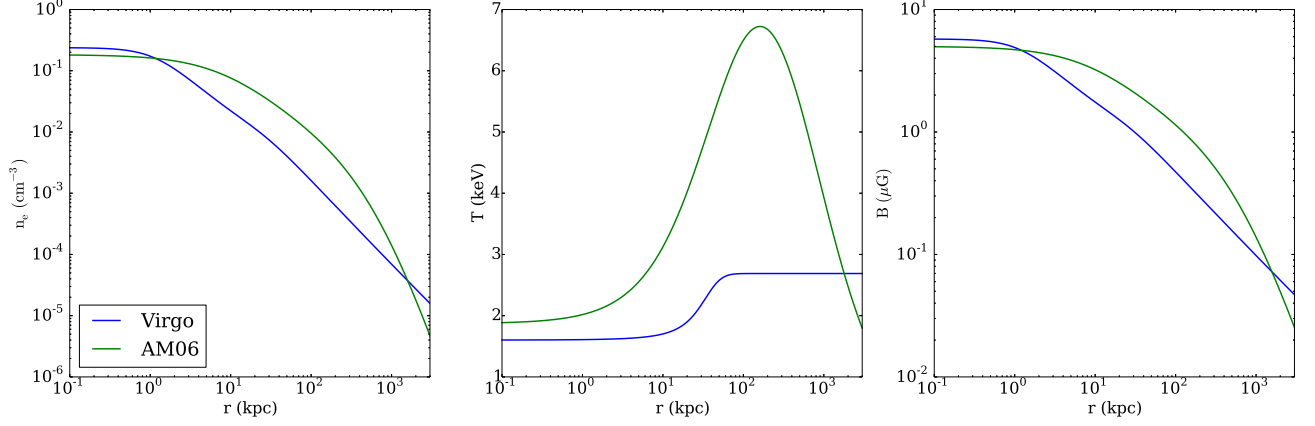


FIG. 1.— Initial profiles of the density, temperature, and magnetic field strength for both cluster models.

where μ is the dynamic viscosity coefficient. To illustrate the physics behind anisotropic (Braginskii) viscosity, we will follow a more detailed derivation. Equation (2) may be written in an alternative form:

$$\frac{\partial(\rho \mathbf{v})}{\partial t} + \nabla \cdot (\rho \mathbf{v} \mathbf{v} + \mathbf{P}) = \rho \mathbf{g}, \quad (8)$$

where \mathbf{P} is the total (thermal + magnetic) pressure tensor:

$$\mathbf{P} = \left(p_{\perp} + \frac{B^2}{8\pi} \right) \mathbf{I} - \left(p_{\perp} - p_{\parallel} + \frac{B^2}{4\pi} \right) \hat{\mathbf{b}} \hat{\mathbf{b}}, \quad (9)$$

p_{\perp} (p_{\parallel}) is the thermal pressure perpendicular (parallel) to the magnetic field, and $\hat{\mathbf{b}} = \mathbf{B}/B$ is the unit vector in the direction of the magnetic field. The total thermal pressure satisfies

$$p = \frac{2}{3} p_{\perp} + \frac{1}{3} p_{\parallel}. \quad (10)$$

Differences in these two components of the thermal pressure arise from the conservation of the first and second adiabatic invariants for each particle on timescales much greater than the inverse of the ion gyrofrequency, Ω_g^{-1} (Chew et al. 1956). When the ion-ion collision frequency ν_{ii} is much larger than the rates of change of all fields, an equation for the pressure anisotropy can be obtained by balancing its production by adiabatic invariance with its relaxation via collisions (cf. Schekochihin et al. 2005):

$$p_{\perp} - p_{\parallel} = 0.960 \frac{p_i}{\nu_{ii}} \frac{d}{dt} \ln \frac{B^3}{\rho^2}, \quad (11)$$

where p_i is the thermal pressure of the ions. The ion dynamic viscosity coefficient for the ICM is given by (Spitzer 1962; Braginskii 1965; Sarazin 1988)

$$\begin{aligned} \mu &= 0.960 \frac{n_i k_B T}{\nu_{ii}} \\ &\approx 2.2 \times 10^{-15} \frac{T^{5/2}}{\ln \Lambda_i} \text{ g cm}^{-1} \text{ s}^{-1}, \end{aligned} \quad (12)$$

where the temperature T is in Kelvin and $\ln \Lambda_i$ is the ion Coulomb logarithm, which is a weak function of ρ and T ; for simplicity we follow Roediger et al. (2013a)

by approximating $\ln \Lambda_i = 40$, appropriate for conditions in the ICM. The kinematic coefficient of viscosity $\nu = \mu/\rho$. Using Equations (1) and (4) to replace the time derivatives of density and magnetic field strength with velocity gradients, Equation (11) may be written as

$$p_{\perp} - p_{\parallel} = 3\mu \left(\hat{\mathbf{b}} \hat{\mathbf{b}} - \frac{1}{3} \mathbf{I} \right) : \nabla \mathbf{v}. \quad (13)$$

It can then be shown that Equations (2) and (8) are equivalent, with the resulting viscous flux for the anisotropic (Braginskii) case being

$$\Pi_{\text{aniso}} = -3\mu \left(\hat{\mathbf{b}} \hat{\mathbf{b}} - \frac{1}{3} \mathbf{I} \right) \left(\hat{\mathbf{b}} \hat{\mathbf{b}} - \frac{1}{3} \mathbf{I} \right) : \nabla \mathbf{v}. \quad (14)$$

These two different fluxes (isotropic, Eqn. 7, and anisotropic, Eqn. 14) are implemented in our different simulations. For the isotropic cases, we model viscosities less than the Spitzer value by including a multiplicative suppression factor f .

We also include anisotropic thermal conduction in some of our runs. The heat flux due to thermal conduction by electrons is given by

$$\mathbf{Q} = -\kappa \hat{\mathbf{b}} \hat{\mathbf{b}} \cdot \nabla T, \quad (15)$$

where the conductivity coefficient (Spitzer 1962; Braginskii 1965; Sarazin 1988)

$$\begin{aligned} \kappa &= 3.2 k_B \frac{n_e k_B T}{m_e \nu_{ee}} \\ &\approx 1.84 \times 10^{-5} \frac{T^{5/2}}{\ln \Lambda_e} \text{ erg cm}^{-1} \text{ s}^{-1} \text{ K}^{-1}, \end{aligned} \quad (16)$$

where ν_{ee} is the electron-electron collision frequency and $\ln \Lambda_e = 40$ is the electron Coulomb logarithm. In this model, the conduction proceeds at full Spitzer rate parallel to the field lines, and is zero perpendicular to the lines. The corresponding thermal diffusivity $\chi = \kappa T/p$. Following Cowie & McKee (1977), we include the effect of conduction saturation whenever the characteristic length scale associated with the temperature gradient is smaller than the electron mean free path (although in the bulk of the ICM this effect is insignificant).

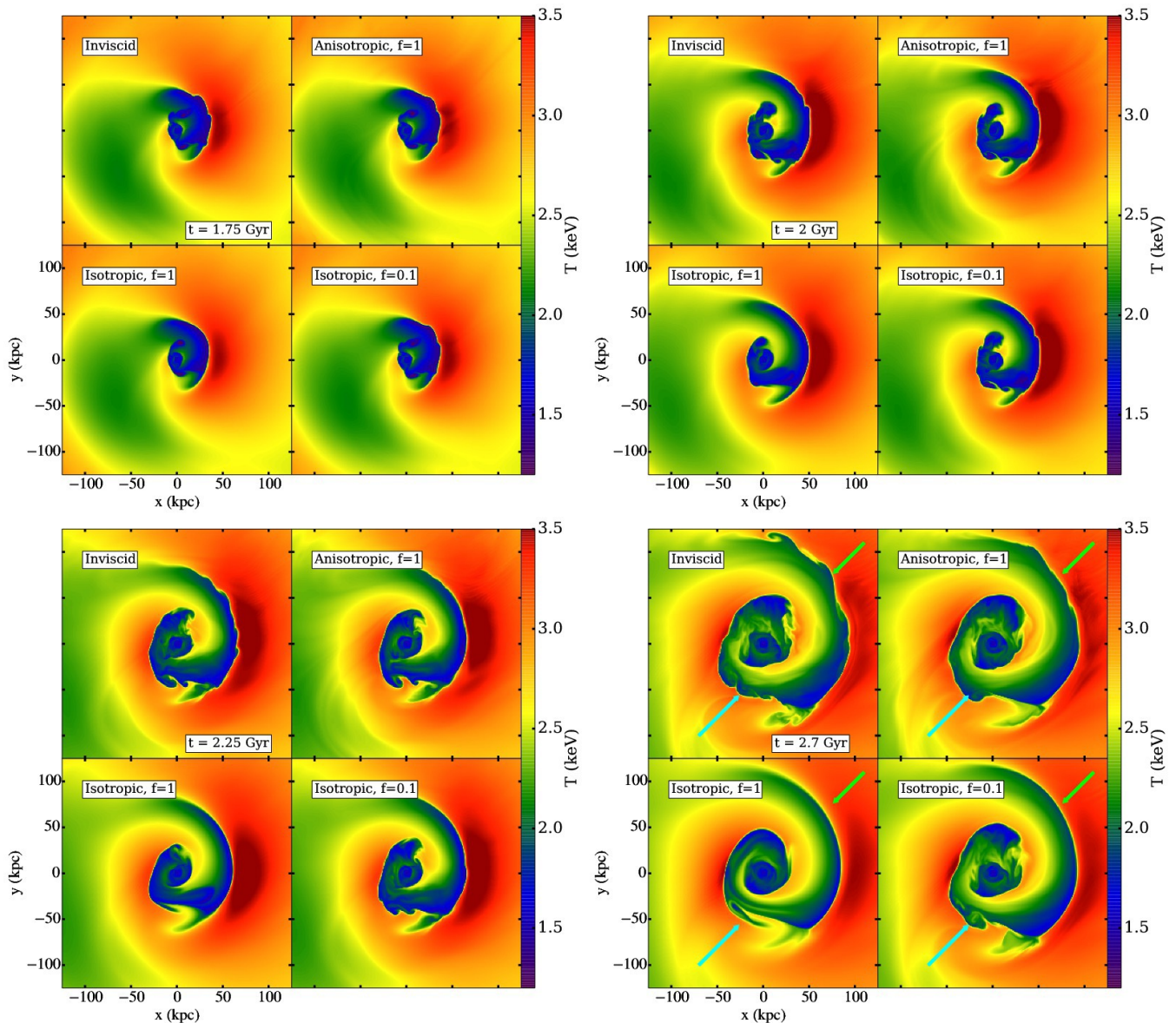


FIG. 2.— Slices of temperature through the center of the “Virgo” simulation domain at times $t = 1.75, 2.0, 2.25$, and 2.7 Gyr, the latter of which corresponds to the time identified as closely matching the merger state of the Virgo cluster in the simulations of Roediger et al. (2011) and Roediger et al. (2013a). Arrows mark the positions of cold fronts with morphologies that are altered by viscosity.

2.2. Code

We performed our simulations using **Athena** 4.1, a parallel conservative magnetohydrodynamic (MHD) astrophysical simulation code (Stone et al. 2008). The MHD algorithms in **Athena** are detailed in Gardiner & Stone (2005, 2008). The directionally unsplit corner transport upwind (CTU) integration method and the HLLD Riemann solver are used in all of our simulations, with third-order (piecewise parabolic Colella & Woodward 1984) reconstruction.

We included anisotropic conduction and Braginskii viscosity following the approaches of Sharma & Hammett (2007), Dong & Stone (2009), Parrish et al. (2012), and Kunz et al. (2012). The conductive and viscous fluxes are implemented via operator splitting, with mono-tonized central (MC) limiters applied to the fluxes to

preserve monotonicity. The latter ensures that unphysical transport of energy and momentum does not occur in the presence of steep gradients.⁵ Since these diffusive processes are modeled by explicit time-stepping methods, they have very restrictive Courant-limited timesteps $\propto (\Delta x)^2$. For this reason, we choose to accelerate the calculation via the method of super-time-stepping (STS,

⁵ Our implementation differs slightly from that presented in the Appendix of Parrish et al. (2012). Those authors applied a slope limiter \mathcal{L} to arithmetically averaged transverse velocity gradients, which are located at cell corners (e.g. at $i - 1/2, j + 1/2$ – see their eq. A5 and fig. A1), in order to obtain the face-centered quantities (e.g. at $i - 1/2, j$) necessary to compute the viscous fluxes. They claim that this interpolation preserves monotonicity. By contrast, we do not arithmetically average at any step. We compute cell-corned transverse velocity gradients by slope limiting face-centered gradients (e.g. those at $i - 1, j + 1/2$ and $i, j + 1/2$), and then slope limit those quantities to compute the viscous fluxes on the cell

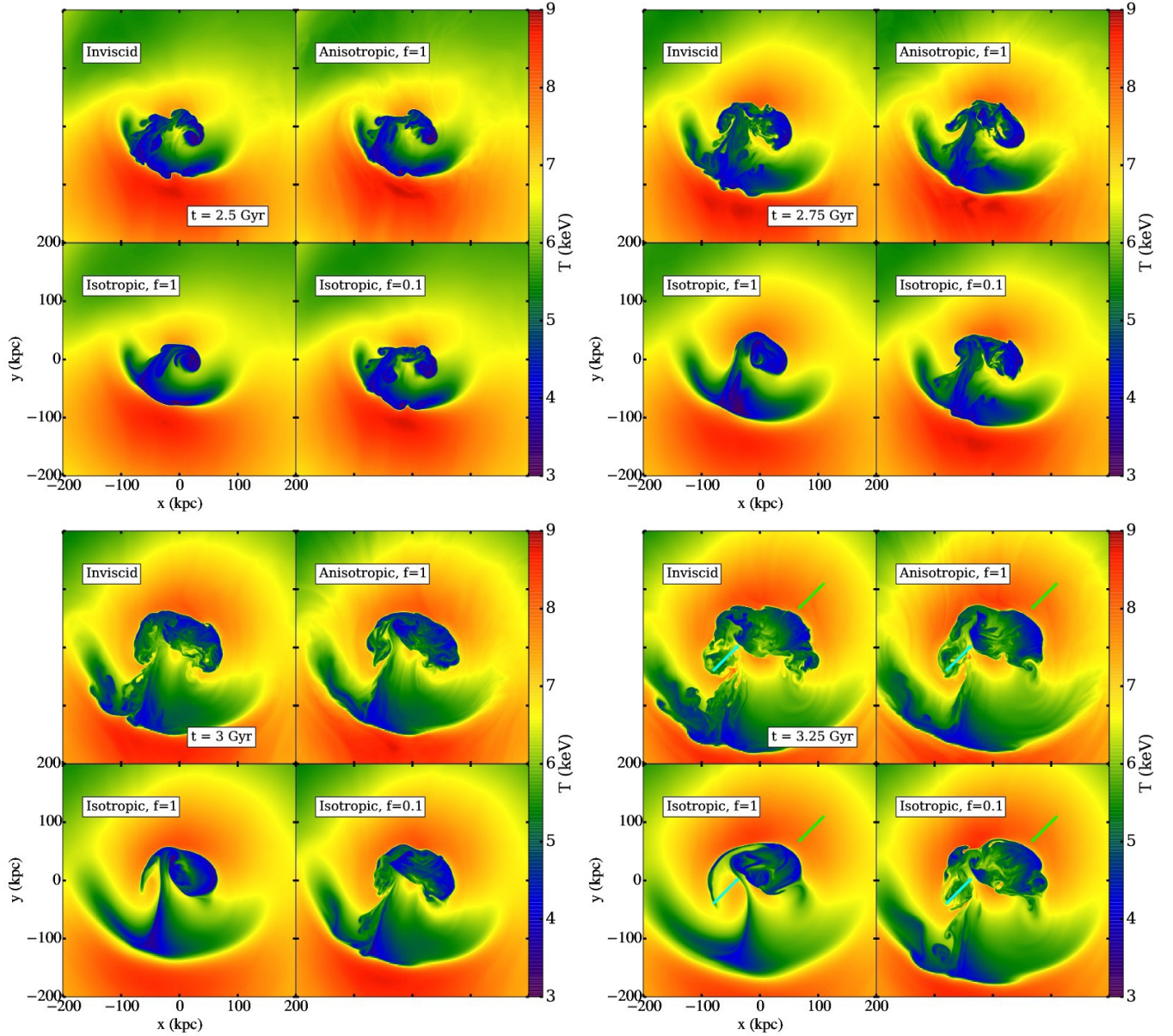


FIG. 3.— Slices of temperature through the center of the “AM06” simulation domain at times $t = 2.5, 2.75, 3.0$, and 3.25 Gyr. Arrows mark the positions of cold fronts with morphologies that are altered by viscosity.

Alexiades et al. 1996). Since we are only concerned in this work with the effects of ICM microphysics on the cold fronts, we do not explicitly include the effects of radiative cooling during the simulation, though our initial condition implicitly assumes that the cool core was originally formed by such cooling.

faces. Using our algorithm, their eq. A4 would instead read

$$\left(\frac{\partial v_x}{\partial y}\right)_{i-\frac{1}{2},j} = \mathcal{L} \left\{ \mathcal{L} \left[\left(\frac{\partial v_x}{\partial y}\right)_{i,j+\frac{1}{2}}, \left(\frac{\partial v_x}{\partial y}\right)_{i-1,j+\frac{1}{2}} \right], \mathcal{L} \left[\left(\frac{\partial v_x}{\partial y}\right)_{i,j-\frac{1}{2}}, \left(\frac{\partial v_x}{\partial y}\right)_{i-1,j-\frac{1}{2}} \right] \right\}.$$

This interpolation preserves monotonicity and is more in line with the original monotonicity-preserving algorithm developed for anisotropic conduction by Sharma & Hammett (2007, their eq. 17).

2.3. Initial Conditions

We model two cluster merger scenarios, both drawn from previous investigations. The first is the setup from Roediger et al. (2011) and Roediger et al. (2013a), which we dub “Virgo”. Virgo is modeled as a cool-core cluster with $M \sim 2 \times 10^{14} M_\odot$ and $T_X \sim 2$ keV. The gas-less subcluster is modeled as a Hernquist dark-matter (DM) halo with a mass of $2 \times 10^{13} M_\odot$. The trajectory results in a closest passage of the subcluster of ≈ 100 kpc at time $t = 1.0$ Gyr in the simulation.⁶ The moment identified by Roediger et al. (2011) as most consistent with the shape and size of the Virgo cold fronts is $t = 2.7$ Gyr in our simulations.

⁶ In contrast to (Roediger et al. 2011) we define $t = 0.0$ at the beginning of the simulation instead of at the core passage.

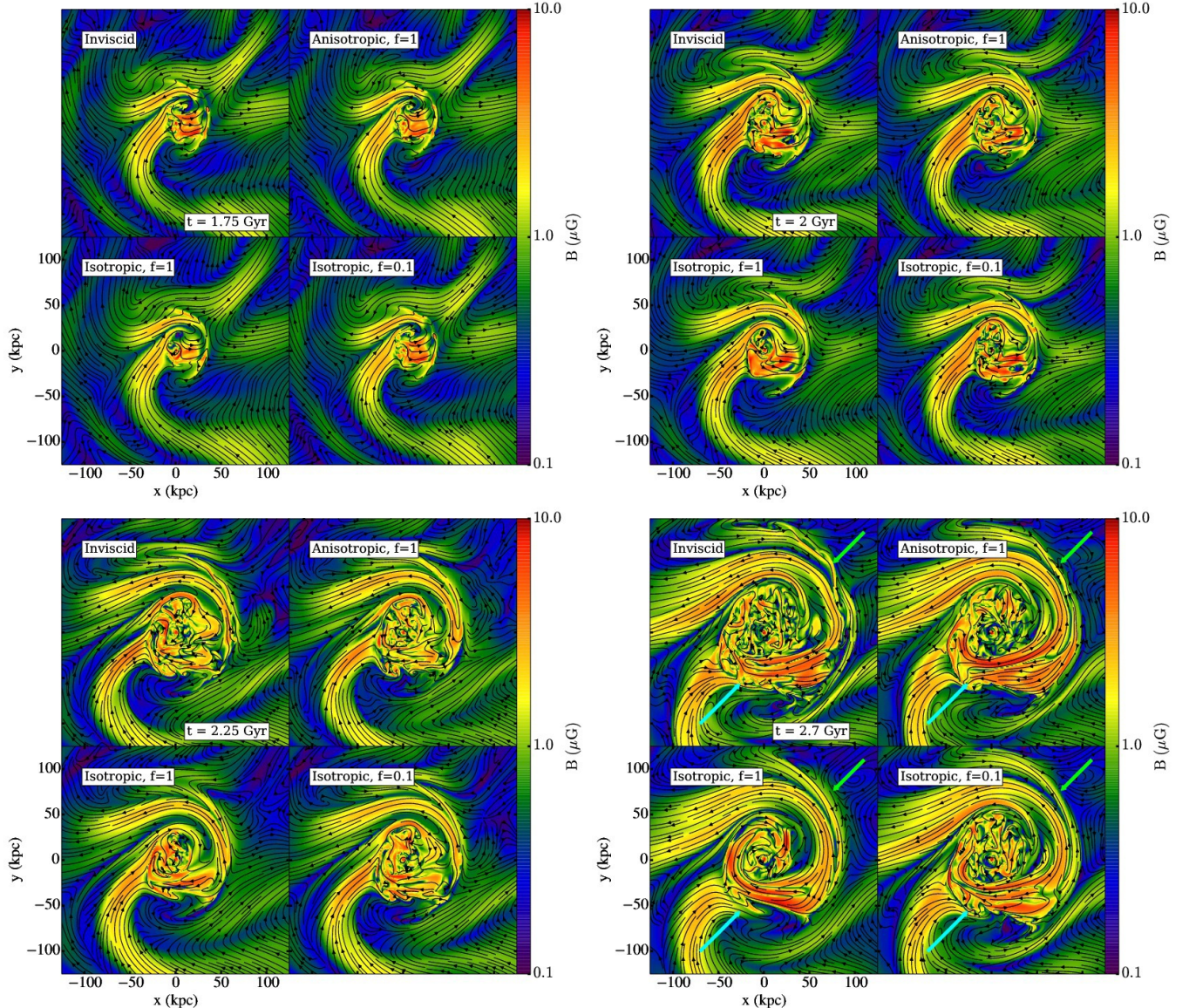


FIG. 4.— Slices of magnetic-field strength through the center of the “Virgo” simulation domain at times $t = 1.75, 2.0, 2.25$, and 2.7 Gyr, with magnetic-field lines in the plane overlaid. The final time corresponds to the epoch identified as closely matching the merger state of the Virgo cluster in the simulations of Roediger et al. (2011) and Roediger et al. (2013a). Arrows mark the positions of cold fronts with morphologies that are altered by viscosity.

The second merger scenario is identical to our previous setup in ZML11 and Z13, which was originally derived from Ascasibar & Markevitch (2006). In this case, the cool-core cluster is more massive ($M \sim 10^{15} M_{\odot}$) and hotter ($T \sim 7$ keV), resembling A2029 (though not exactly reproducing it). The gas-less subcluster is 5 times less massive than the main cluster and approaches it with an initial impact parameter of $b = 500$ kpc. We will refer to this setup as “AM06”.

The gravitational potential on the grid is the sum of two collisionless “rigid bodies” corresponding to the contributions to the potential from both clusters. This approach to modeling the potential is used for simplicity and speed over solving the Poisson equation for the matter distribution, and is an adequate approximation for our purposes. It is the same approach that

we used in ZML11, and is justified and explained in Roediger & Zuhone (2012).

The tangled magnetic field of the cluster is set up in an similar way to the simulations of ZML11 and Z13. We use a radial profile for the magnetic field strength of $B = B_0[\rho(r)/\rho_0]^{\eta}$ with $\eta = 0.5$ (Bonafede et al. 2010). The average magnetic field strength in the core region corresponds to $\beta = p_{\text{th}}/B \sim 1000 - 1500$, which is on the weaker end of the parameter space from ZML11. This low field strength was chosen to ensure the development of K-H instabilities in order to determine the effect of viscosity on their development. For the three-dimensional tangled structure of the initial magnetic field, we follow the approach of Ruszkowski et al. (2007, 2008) and Ruszkowski & Oh (2010), and we refer the reader to those papers for the details. Figure 1 shows the initial ra-

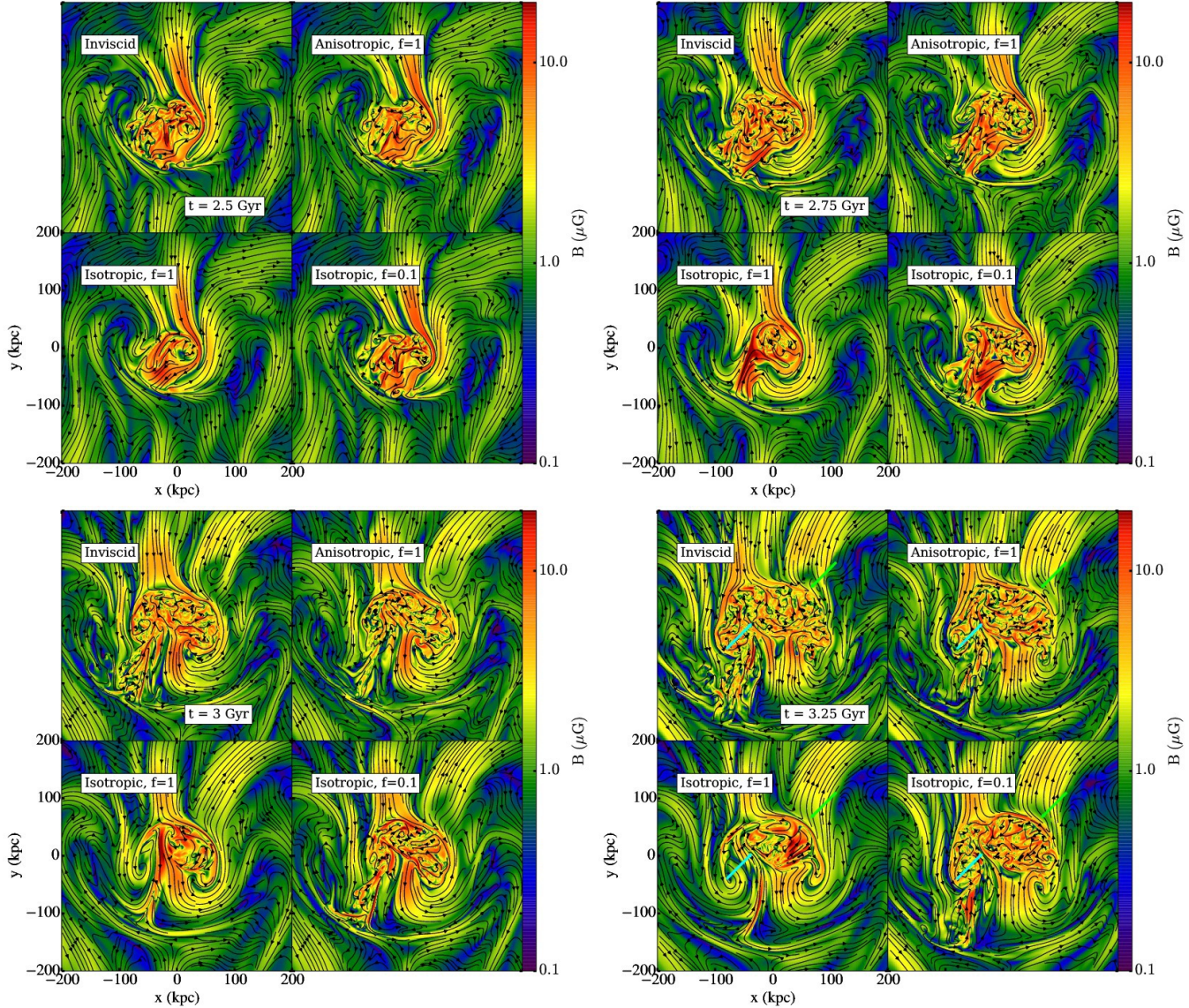


FIG. 5.— Slices of magnetic-field strength through the center of the “AM06” simulation domain at times $t = 2.5, 2.75, 3.0$, and 3.25 Gyr, with magnetic-field lines in the plane overlaid. Arrows mark the positions of cold fronts with morphologies that are altered by viscosity.

dial profiles of density, temperature, and magnetic-field strength for both clusters.

For all of the simulations, we set up the main cluster within a cubical computational domain of width $L = 4$ Mpc on a side. We employ static mesh refinement (SMR), with 256 cells on a side on the top-level domain and five smaller domains at increasing levels of refinement, each half the size of the domain just above it, centered on the cluster potential minimum. This results in a finest cell size of $\Delta x = 0.98$ kpc within a region of $l^3 = (250 \text{ kpc})^3$. Appendix A details the results of a test where we experiment with higher and lower spatial resolutions. Roediger et al. (2013b) examined the effect of varying resolution on the development of K-H instabilities in a simulation of the ICM, and determined that the gross morphologies of the K-H rolls is captured well down to resolutions of 32 cells per perturbation wavelength, a wavelength of $\lambda \sim 32$ kpc in our simulations (for further

discussion of the effects of resolution see Section 4.2).

Similar to the approach taken in Z13 for simulations with diffusive effects (viscosity and/or conduction), we switch on these effects at the pericentric passage ($t = 1.0$ Gyr in the case of the “Virgo” simulations and $t \sim 1.5$ Gyr in the case of the “AM06” simulations). This is just before the onset of sloshing, and allows us to examine the effects of these processes on the sloshing cold fronts without any significant change in our initial condition of the main cluster that would occur if these effects (particularly conduction) were switched on.

For these two cluster models, we perform four simulations each with different types of viscosity. Also, for each model we perform two additional simulations with anisotropic thermal conduction, one of the two including Braginskii viscosity. In addition, to see the effect of viscosity separate from that of the magnetic field for the same cluster setup, we also ran unmagnetized runs with

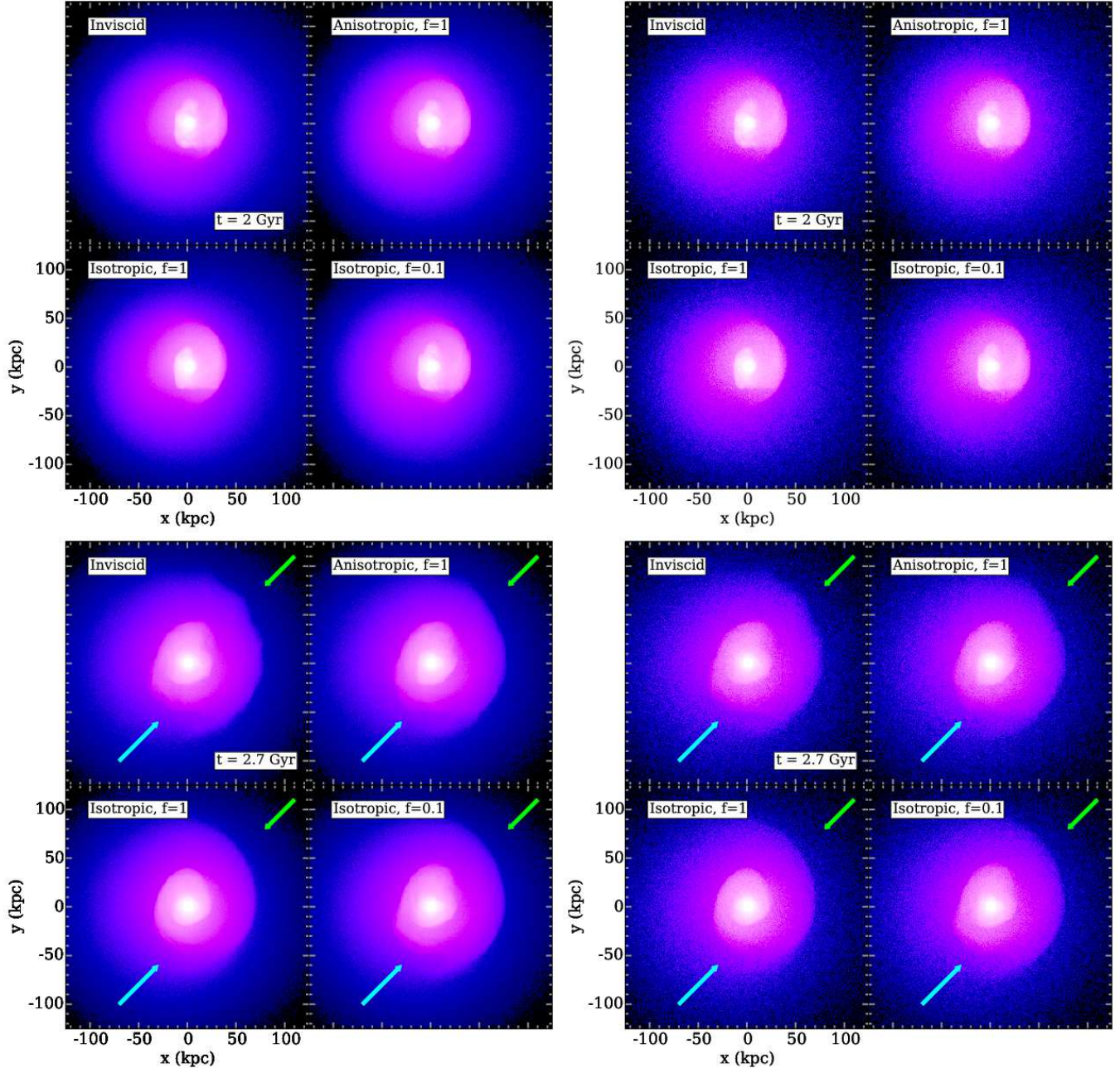


FIG. 6.— Synthetic X-ray counts images of the “Virgo” cluster for the four different viscosity simulations at times $t = 2.0$ and 2.7 Gyr. Left panels: 300-ks exposure. Right panels: 30-ks exposure. Arrows mark the positions of cold fronts with morphologies that are altered by viscosity.

and without viscosity of both setups (detailed in Section 4.6). These are all exploratory runs, not intended to cover the full parameter space of the viscosity and magnetic field values; we will try to reproduce particular observed clusters in a future work.

3. RESULTS

3.1. Temperature and Magnetic-Field Maps

We begin by visually examining the development of K-H instabilities at cold front surfaces in slices through the center of the simulation domain in the merger plane. Figures 2 and 3 show temperature slices for the two clusters

at various times in the different simulations. The *inviscid* simulations quickly develop K-H instabilities at the cold front surfaces, which continue to grow and develop as the simulations progress. These instabilities generate turbulence (to be discussed in Section 3.3) and significant small-scale structure in temperature. In the *anisotropic* and *isotropic* $f = 0.1$ simulations, the same instabilities develop at early times, but as the cold fronts expand, these are progressively damped out by viscosity. We mark the positions of cold fronts with different morphology in the different simulations with arrows. However, there are still some locations along the fronts where

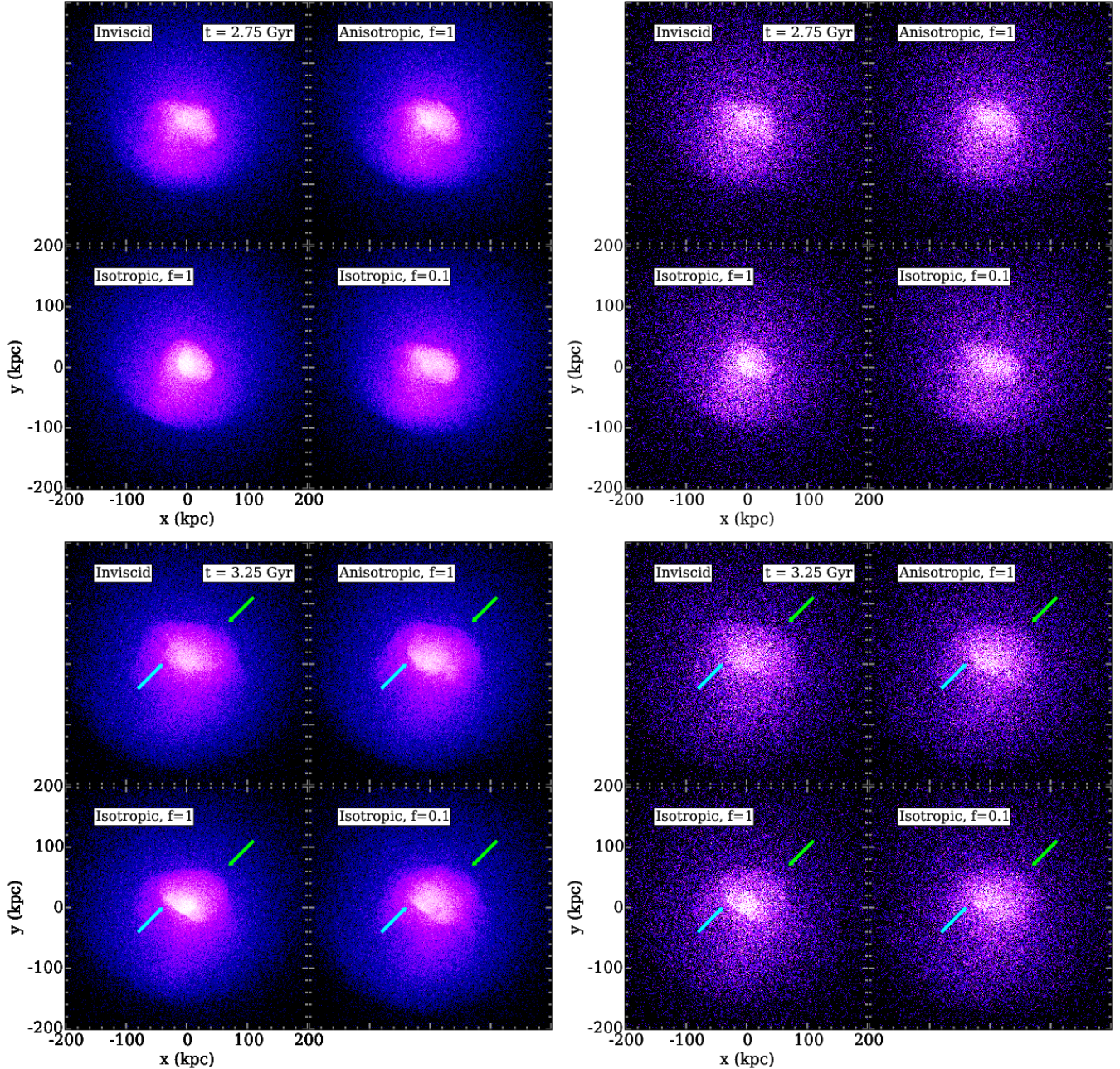


FIG. 7.— Synthetic X-ray counts images of the “AM06” cluster for the four different viscosity simulations at times $t = 2.75$ and 3.25 Gyr. Left panels: 300-ks exposure. Right panels: 30-ks exposure. Arrows mark the positions of cold fronts with morphologies that are altered by viscosity.

there are indications of instability, as well as some small-scale temperature fluctuations within the envelope of the cold fronts. In the case of the *isotropic*, $f=1$ simulations, no K-H instabilities or small-scale temperature structures develop at all during the course of the simulations.

Figures 4 and 5 show slices of the magnetic-field strength for the two clusters at the same times for the different simulations. The overall evolution of the magnetic field is very similar in all the simulations, but there are some differences. The magnetic draping layers that occur along cold front surfaces are disrupted by K-H instabilities in the *inviscid* simulations, whereas viscosity

results in magnetic-field layers that are more smooth (see the arrows in the figures), though there is not a perfect wrapping of fields around the cold fronts in any of the simulations (we will examine the consequences of this for anisotropic thermal conduction in Section 3.4). As viscosity is increased, there is less small-scale structure in the magnetic field.

3.2. Synthetic X-ray Observations

To make closer comparisons with observations of cold fronts in actual clusters, we construct synthetic *Chandra* observations. We generate X-ray photons from an

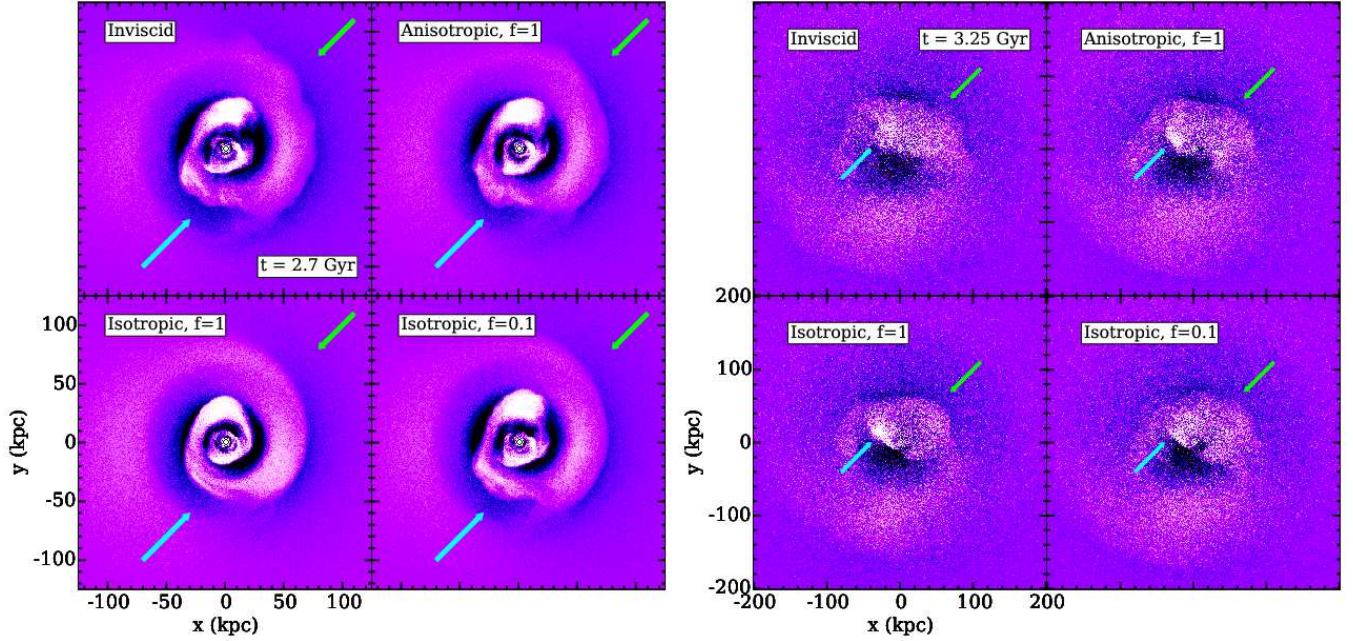


FIG. 8.— Synthetic X-ray residual images (from the 300-ks exposures, after subtraction of the azimuthally averaged profile) of the two clusters for the four different viscosity simulations at late times. Left panels: “Virgo” model. Right panels: “AM06” model.

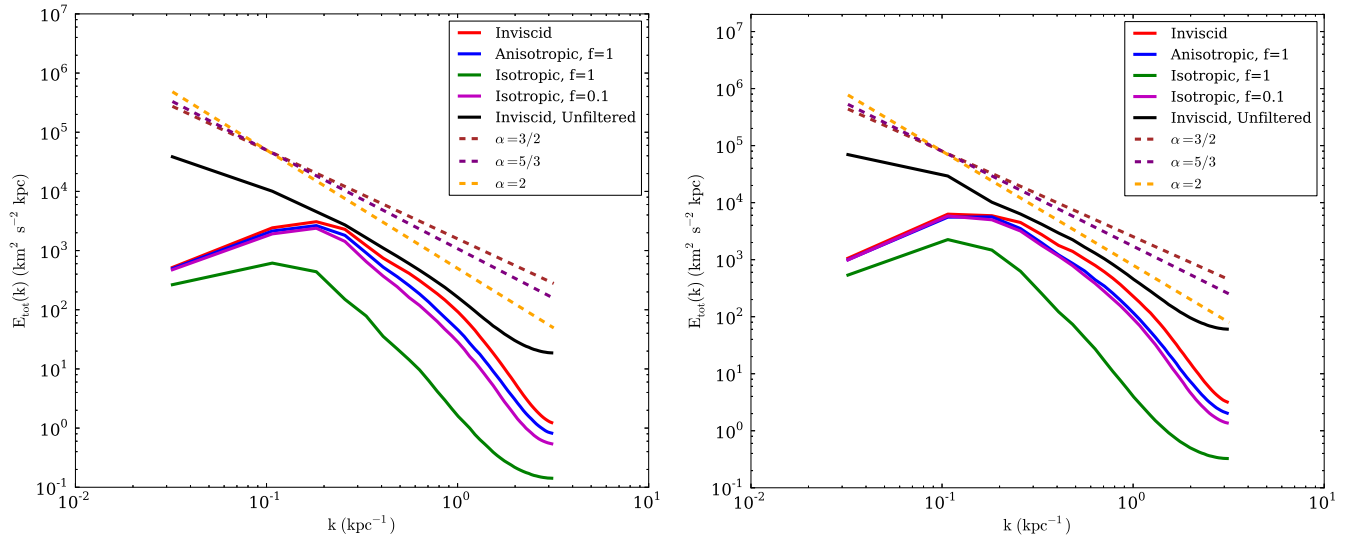


FIG. 9.— Velocity power spectra for the “Virgo” simulations at time $t = 2.7$ Gyr (left panel) and the “AM06” simulations at time $t = 3.25$ Gyr (right panel).

APEC model (Smith et al. 2001) of a thermal gas with $Z = 0.3Z_{\odot}$ for each simulation cell within a radius of $R = 250$ kpc from the cluster potential minimum.⁷ We also apply Galactic absorption assuming $N_H = 10^{21}$ cm². Our procedure for generating these observations is outlined in detail in Appendix B. To generate an approximate number of counts that would be expected from a mosaic of *Chandra* observations of each of our simulated clusters, we use the on-axis effective area curve of

⁷ This radius contains the cold fronts at all epochs that we simulate; we find that including gas at larger radii in the synthetic images does not affect our conclusions.

the ACIS-S3 chip. For the “Virgo” simulations, we use the actual redshift of the Virgo cluster, $z = 0.0036$, and for the “AM06” simulations, we choose a redshift of $z = 0.1$. The images have been blocked so that the pixels correspond to the size of the finest simulation cell size, $\Delta x = 0.98$ kpc.⁸ To determine the effect of photon statistics, we simulate two different exposures, 300 ks and 30 ks.

Figures 6 and 7 show the X-ray counts images of the

⁸ In the “AM06” case, this happens to correspond roughly to the *Chandra* pixel size (0.492”) at $z = 0.1$. In the “Virgo” case, the *Chandra* pixels are ~ 0.04 kpc, much smaller than our cell size.

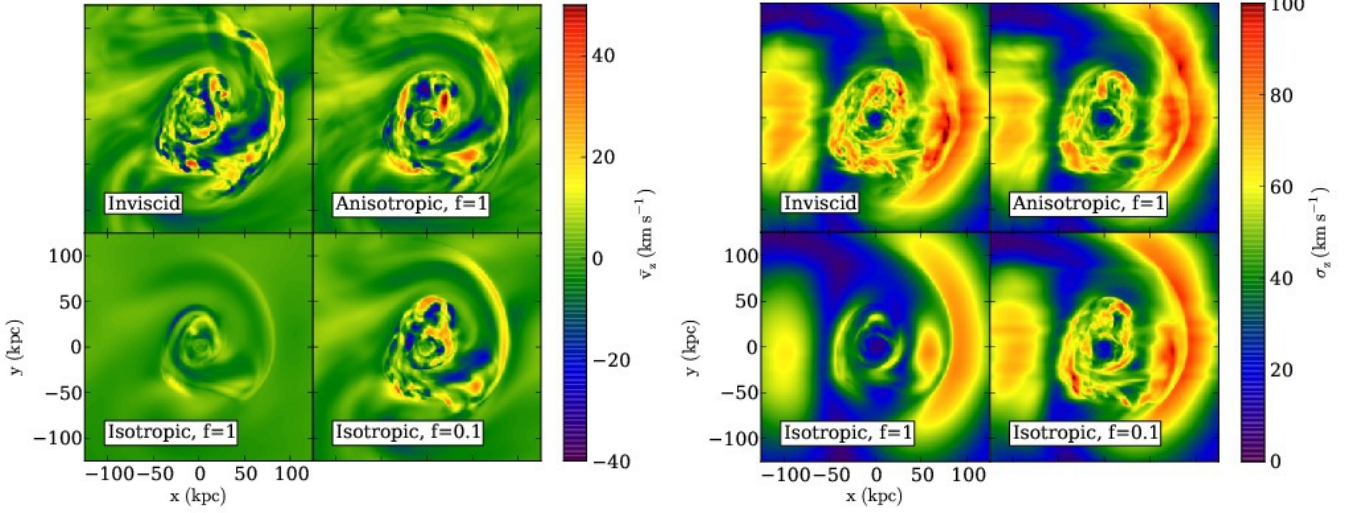


FIG. 10.— Emission-weighted line-of-sight velocity along the z -axis for the “Virgo” simulations at time $t = 2.7$ Gyr. Left panels: velocity mean, right panels: velocity dispersion, which is a good measure of turbulence (ZuHone et al. 2013).

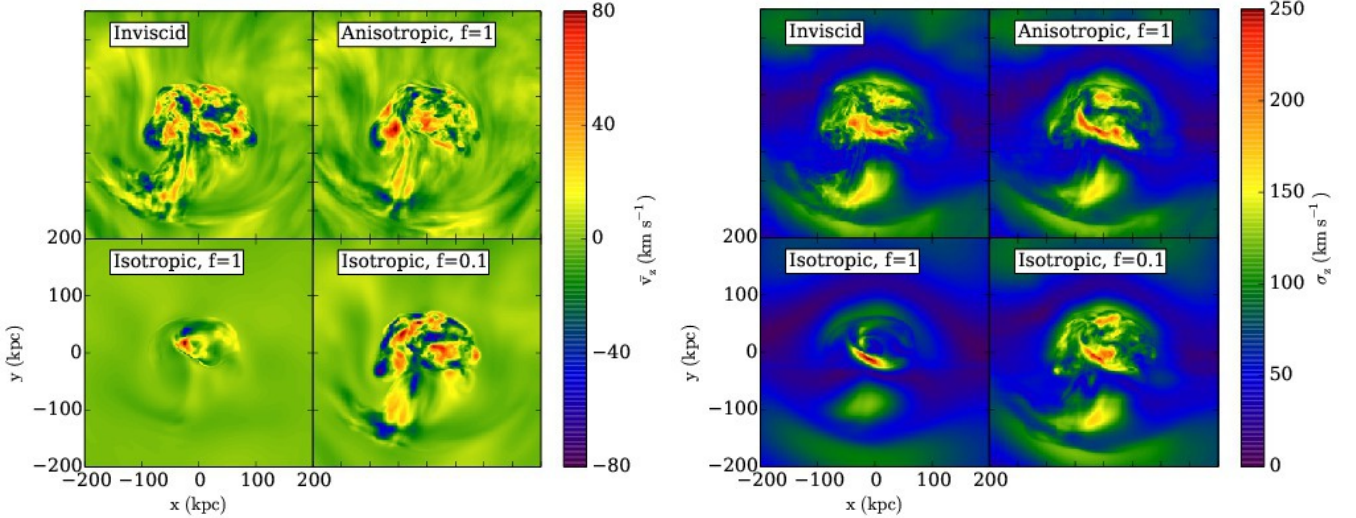


FIG. 11.— Emission-weighted projections of the line-of-sight velocity while looking along the z -axis for the “AM06” simulations at time $t = 3.25$ Gyr. Left panels: velocity mean, right panels: velocity dispersion.

two model clusters at different epochs and for different exposure times. Projection effects and Poisson noise make the interpretation of these images more difficult than for the temperature slices. It is clear that long exposures (in our case, ~ 300 ks) are needed for determining the amount of K-H disruption at the cold front surfaces. In the 30-ks exposures, it is much more difficult to make distinctions between the cold fronts in the simulations due to poor statistics. For the rest of this section, we will focus on the 300-ks exposures.

In the *inviscid* simulations, the presence of K-H instabilities along the cold front surfaces is readily apparent from the X-ray images. By contrast, in the *isotropic*, $f=1$ simulations, the cold front arcs are completely smooth in appearance. In the *isotropic*, $f=0.1$ and *anisotropic* simulations, while the cold front surfaces are mostly smooth, small indications of instability are visible. Some

fronts that appear in the viscous simulations are so disrupted in the *inviscid* simulations that they are no longer technically cold fronts (one example is in the “AM06” simulations, indicated by the cyan arrow in Figure 7). Another indicator of cold front instability is the overall shape of the cold fronts. Unstable fronts tend to have a “boxy” shape, due to the development of the instability over the curved surface, whereas fronts stabilized by viscosity appear more round (a fact previously pointed out by Roediger et al. 2012). This is most evident in the “AM06” case.

The characteristics of the cold front structures may be seen more clearly by looking at the surface brightness residuals instead of the surface brightness itself. Figure 8 shows the surface brightness residuals for both models at a late epoch, generated by computing an azimuthally averaged radial profile of the counts from the 300-ks obser-

vation and subtracting the corresponding image from the original image. As in Figures 6 and 7, the arrows mark the positions of cold fronts with different morphologies in the different simulations. The difference in the degree of K-H disruption can be more clearly seen. In particular, it is obvious from the right panel of Figure 8 that the cold front at the inner radius (indicated by the cyan arrow) is essentially impossible to discern even in the residual image in the *inviscid* case.

3.3. The Effect of Viscosity on Sloshing-Driven Turbulence

Viscosity can have an effect on turbulence driven by sloshing by damping out turbulent motions on the smallest length scales. Future X-ray telescopes such as *Astro-H*⁹ and *Athena+*¹⁰ will be able to measure turbulence and bulk motions from the line shift and line widths of spectral lines (Inogamov & Sunyaev 2003; Sunyaev et al. 2003). It is instructive to determine the effect of our different viscosity models on the turbulence driven by sloshing.

A straightforward way to distinguish the turbulent velocity field between the different models is to compare the velocity power spectra. The sloshing motions themselves complicate matters, since the velocity jumps across the cold fronts impose a $\sim k^{-2}$ signature on the power spectrum at all wavenumbers k . Since the bulk of the motion in the simulation is in the sloshing motions, this signal dominates. This reduces to the more general problem of separating turbulence from bulk motions in hydrodynamic simulations, a subject of previous investigations (Vazza et al. 2012; ZuHone et al. 2013). To carry out this decomposition, we use the procedure outlined in Vazza et al. (2012), which uses a multi-scale filtering scheme to iteratively converge on the mean velocity field around each cell, which is then subtracted from the total velocity to get the turbulent component. As noted by ZuHone et al. (2013), carrying out the filtering procedure naively on the velocity field from sloshing cold fronts will not completely remove the effect of the bulk motions, because the velocity differences across the cold fronts will result in the local mean velocity changing discontinuously across these surfaces. Vazza et al. (2012) noted the same difficulty with shock fronts, and proposed filtering on the skew of the local velocity field as a way to avoid these difficulties. We adopt the same approach here for our simulations.

Figure 9 shows the filtered (“turbulent”) velocity power spectrum as a function of wavenumber k for all of the simulations, as well as the unfiltered velocity power spectrum for the *inviscid* simulations (for comparison). The *anisotropic* simulations with the full Braginskii viscosity result in a very modest reduction of the turbulent power, whereas for the *isotropic* simulations with full Spitzer viscosity the turbulent power is reduced by more than an order of magnitude.

Figures 10 and 11 show the emission-weighted projected line-of-sight mean velocity and line-of-sight velocity dispersion along the z -axis of the simulation domain for all of the simulations. For this exercise, we have not filtered out the bulk motions. The projections

of the two *inviscid* simulations show evidence of turbulence in small-scale random velocity fluctuations. In the *anisotropic* simulations, turbulence is somewhat reduced, but the small-scale velocity fluctuations are still present. This is also the case for the *isotropic*, $f = 0.1$ simulations. In the *isotropic*, $f = 1$ simulations, essentially all of the small-scale motions are absent.

We also find in all of our simulations that significant velocity dispersions may be measured along the line of sight that do not correspond to turbulent motions but instead to large variations in the bulk motion along the line of sight. Though we have determined the dispersion here by simply computing it from the velocity field itself, this effect will also show up in the broadening of X-ray spectral lines, which is how turbulence is to be measured. We stress that care must be taken in interpreting the results of future measurements of the width of spectral lines as resulting from turbulence, since it is possible for bulk motions along the line of sight to produce similar signatures. We will examine this effect in the context of a sloshing cool core in more detail in a separate work.

3.4. Simulations with Anisotropic Thermal Conduction

Z13 found that anisotropic thermal conduction acted to smooth out the cold front temperature and density jumps despite the presence of magnetic draping layers. This may be the result of imperfections in the magnetic layers due to field-line tangling from K-H instabilities, resulting in some “leaking” of heat from the hot plasma above the cold front, or to the presence of other regions of hot plasma that are not magnetically isolated from the colder gas inside the fronts (e.g. the spiral-shaped “tongues” of hot gas in between the cold fronts, see Figures 2 and 3). If viscosity acts to prevent the development of K-H instabilities, it is possible that the magnetic draping layers that develop will be more aligned to the smooth cold front surfaces and hence they may be more effective at suppressing conduction than in the *inviscid* case. In Figures 2 and 4, we saw two cold fronts where viscosity has suppressed K-H instabilities and produced magnetic fields more aligned to the cold front surfaces. This hypothesis motivates our simulations with anisotropic thermal conduction and anisotropic viscosity.

We performed two additional simulations for each of our model clusters, one with anisotropic thermal conduction (full Spitzer rate along the field lines and zero across the lines, see Section 2.1) and one with both anisotropic thermal conduction and Braginskii viscosity. Figure 12 shows images of projected temperature constructed at specific epochs for the “Virgo” and “AM06” simulations. In the simulations with anisotropic thermal conduction, though there are still surface brightness gradients at the positions of the cold fronts in the *inviscid* simulations, these gradients have been smoothed out. This is demonstrated more quantitatively in Figure 13, which shows the extracted surface brightness and projected temperature profiles from the colored annular regions in Figure 12. In the simulations with conduction, the gradients are no longer sharp, with or without viscosity, and the radial profiles are essentially identical. The inclusion of Braginskii viscosity appears to have little effect on the smoothing out of cold front jumps by conduction.

⁹ <http://astro-h.isas.jaxa.jp/>

¹⁰ <http://www.the-athena-x-ray-observatory.eu/>

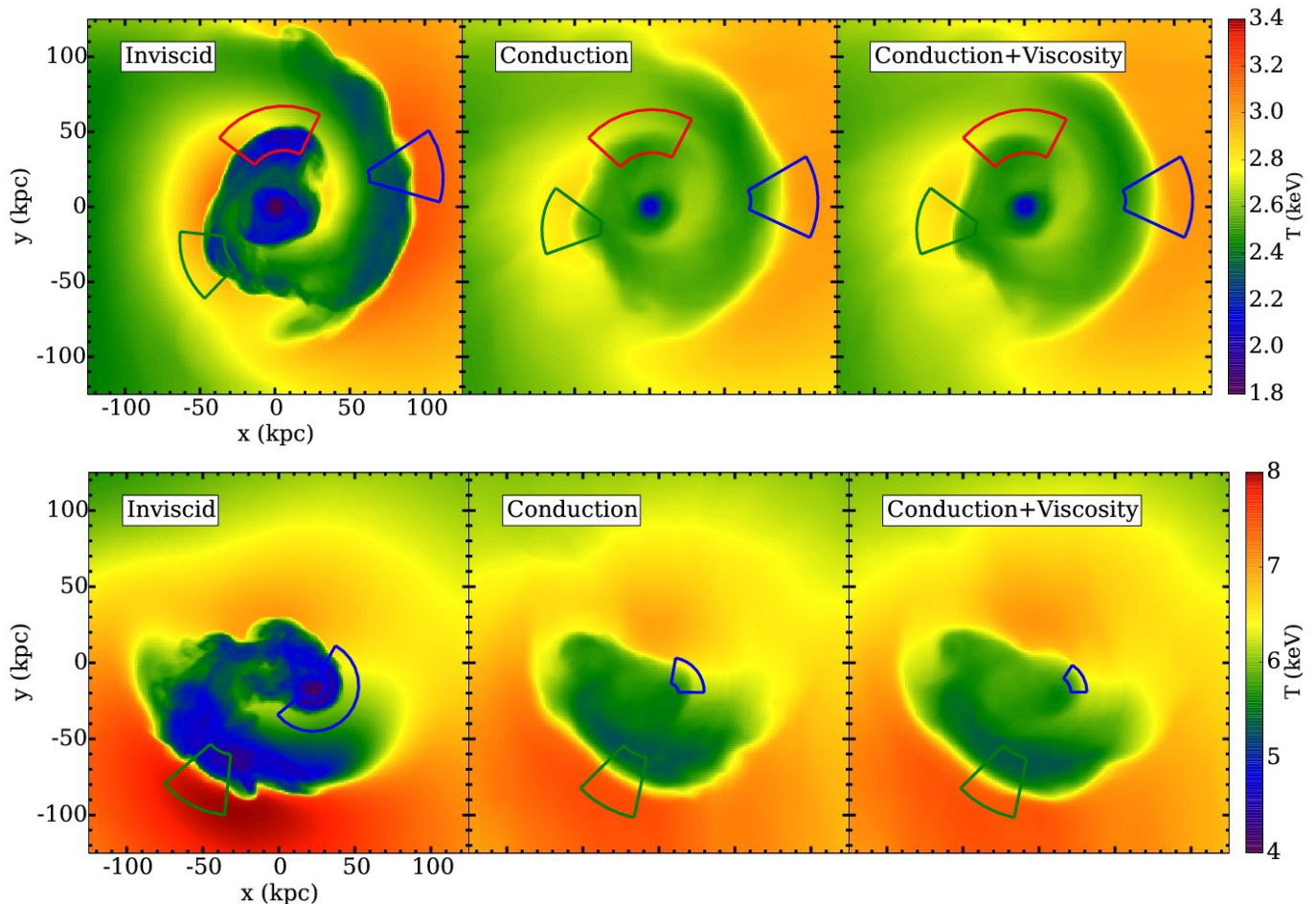


FIG. 12.— Projected “spectroscopic-like” temperature images of the “Virgo” (top) and “AM06” (bottom) clusters for the three different conduction simulations. Regions correspond to the profiles in Figure 13.

4. DISCUSSION

4.1. The Feasibility of Constraining Viscosity from X-ray Observations of Cold Fronts

In our exploratory set of simulations, we have bracketed the range of possibilities for K-H instabilities at sloshing cold fronts for our two examples of low-mass and massive clusters. On the one hand, the cold fronts in our inviscid simulations are very susceptible to K-H instabilities, despite the presence of magnetic fields (this is even more true if magnetic fields are very weak or absent, cf. Section 4.6, ZML11). There appear to be more instabilities in these simulations than we see at cold fronts in actual clusters (a quantitative comparison is forthcoming in our future work). On the other hand, an ICM with an isotropic Spitzer viscosity exhibits no evidence of instabilities at all, which is also contrary to some observations. Our more physically-motivated simulations, with either Braginskii viscosity or a reduced isotropic Spitzer viscosity, appear to qualitatively reproduce the observations in terms of the degree of smoothness of the cold fronts. A quantitative comparison with several well-observed cold fronts will be presented in a subsequent publication. However, from our present study, we infer that it may be difficult to distinguish between an

isotropic “sub-Spitzer” viscosity and anisotropic Braginskii viscosity using X-ray observations alone. The degree of suppression of K-H instabilities at cold front surfaces and the effect on turbulence are both qualitatively similar. From a purely theoretical perspective, Braginskii viscosity is the preferred model because it is known that the ICM is magnetized, and the small Larmor radius of the ions will constrain the momentum transport accordingly.

Other avenues for constraining viscosity in the ICM exist. Dong & Stone (2009) used Braginskii-MHD simulations of buoyant bubbles in a cluster atmosphere to investigate their stability properties. They found that bubble stability was impacted most by the magnetic field geometry. In the core of the Perseus cluster, the smooth shape of some of the H α filaments may indicate the flow around these filaments is laminar and significantly viscous (Fabian et al. 2003). Further simulation studies of these systems and their observations need to be combined with studies of cold fronts to provide better constraints on ICM viscosity.

4.2. Origin of Sloshing-Driven Turbulence and Effects of Resolution

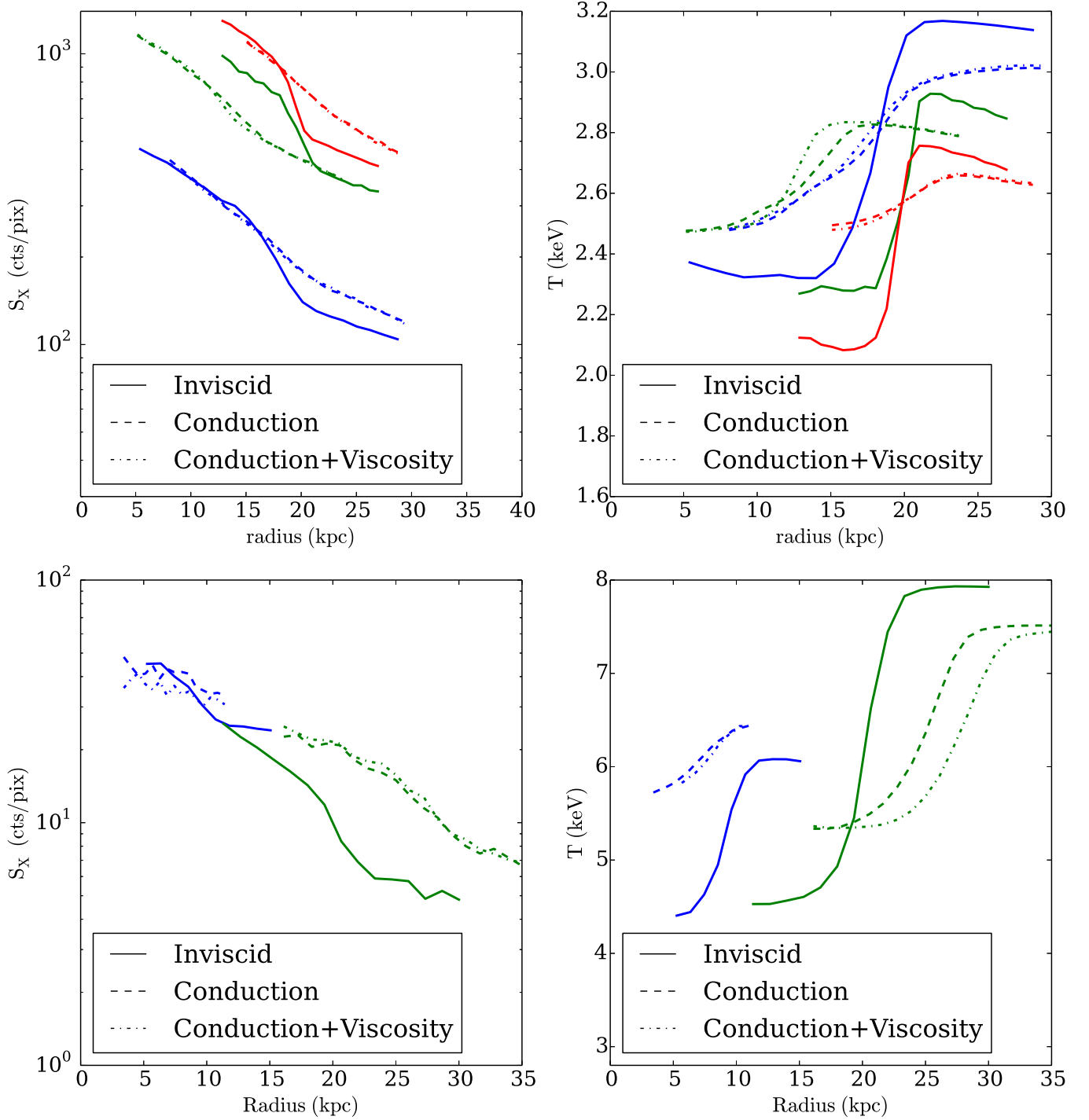


FIG. 13.— Profiles of the surface brightness and projected temperature from the “Virgo” (top) and “AM06” (bottom) clusters for the anisotropic conduction simulations, corresponding to the regions in Figure 12.

The different prescriptions for viscosity in our simulations produce significant differences in the amount of turbulence that is produced. To more fully understand the origin of these differences, it is instructive to examine the relevant scales for turbulence in our simulations. The first is the scale of the sloshing motions themselves, L_0 , which at early times is roughly $L_0 \sim 50$ kpc, increasing at later times to $L_0 \sim 200$ kpc. The second

scale is the scale at which the turbulent cascade is dissipated by viscosity, l_{diss} , assuming a roughly continuous generation of turbulence by the sloshing motions as they expand. For dissipation due to Coulomb collisions, this scale depends on the Reynolds number of the plasma

(e.g., Roediger et al. 2013a):

$$\text{Re} = 7f^{-1} \left(\frac{V_L}{300 \text{ km s}^{-1}} \right) \left(\frac{L_0}{10 \text{ kpc}} \right) \times \left(\frac{n_{\text{th}}}{3 \times 10^{-3} \text{ cm}^{-3}} \right) \left(\frac{T}{3 \text{ keV}} \right), \quad (17)$$

where V_L is the characteristic turbulent eddy velocity on the length scale L_0 , n_{th} is the thermal gas number density, T is the thermal gas temperature, and f is the viscous suppression factor. For Kolmogorov turbulence, $l_{\text{diss}} \sim L_0(\text{Re})^{-3/4}$. For our “Virgo” setup, $\text{Re} \sim 200$ and $l_{\text{diss}} \sim 2 \text{ kpc}$, and for the “AM06” setup, $\text{Re} \sim 100$ and $l_{\text{diss}} \sim 3 \text{ kpc}$, in the relevant region of the cold fronts (assuming $f = 1$ and a value of $L_0 \sim 100 \text{ kpc}$ for the length scale of the sloshing motions). Since these values are very close to the size of our smallest cells, the numerical dissipation dominates, since its effect sets in at a length scale $\sim 8\Delta x$ (ZuHone et al. 2013).

It therefore may seem surprising at first that the different simulations have such wide differences in the amount of turbulence that is produced, since all of the simulations have the same cell size, and in any case the turbulent dissipation from viscosity does not occur except at the smallest scales. However, the relevant scale for generating turbulence, as well as for disrupting the cold front surfaces, is not the dissipation scale of the turbulent cascades, but rather it is the wavelength of the smallest perturbations that will not be damped out by viscosity. In an extensive set of plane-parallel simulations of the K-H instability, Roediger et al. (2013b) determined this scale to be

$$l_{\text{crit}} = 30 \text{ kpc} \left(\frac{\text{Re}_{\text{crit}}}{30} \right) f \left(\frac{V_L}{400 \text{ km s}^{-1}} \right)^{-1} \times \left(\frac{n_{\text{th}}}{10^{-3} \text{ cm}^{-3}} \right)^{-1} \left(\frac{T}{2.4 \text{ keV}} \right)^{5/2} \quad (18)$$

Taking our lead from Roediger et al. (2013b), we assume the critical Reynolds number at which K-H instabilities develop is $\text{Re}_{\text{crit}} \sim 30$. This criterion yields roughly $l_{\text{crit}} \sim 40 \text{ kpc}$ for the outermost cold fronts at late epochs (“Virgo”, $t = 2.7 \text{ Gyr}$, “AM06”, $t = 3.25 \text{ Gyr}$) in both of our models assuming full Spitzer viscosity ($f = 1$). For $f = 0.1$, l_{crit} is an order of magnitude smaller for each model, and a wider range of perturbations that we can resolve in our simulations can become unstable. For Braginskii viscosity, the effective f may be as high as $1/5$ for an isotropically tangled field or even smaller (Nulsen & McNamara 2013), depending on the local magnetic field geometry.

If we examine the cold fronts in the early stages of sloshing (upper panels of Figures 2 and 3), we find that in all cases except the *isotropic*, $f = 1$ simulations that K-H instabilities develop very quickly. These instabilities generate turbulence that eventually develops within the sloshing region in these simulations. In the *isotropic*, $f = 1$ simulation, instabilities never really develop in the first place, the flow is always quite laminar, and as such there is not much turbulence at later stages. Therefore, the most relevant scale that determines the difference between our simulations is l_{crit} , the scale of the smallest perturbations that become unstable. This scale is very well-resolved by our simulations if $f = 1$, $l_{\text{crit}} \sim 40 \text{ kpc}$.

In the $f = 0.1$ case, $l_{\text{crit}} \sim 4 \text{ kpc}$, and this scale is resolved only marginally well (the $8\Delta x$ criterion is not fulfilled), so numerical resolution may start to have a significant effect on our results (see Section 2.3).

4.3. Impact of Unresolved Microphysics on Our Results

When the pressure anisotropy violates the approximate inequalities

$$-\frac{B^2}{4\pi} \lesssim p_{\perp} - p_{\parallel} \lesssim \frac{B^2}{8\pi}, \quad (19)$$

a situation which is expected to occur readily in the ICM (Schekochihin et al. 2005; Lyutikov 2007; Kunz et al. 2011), rapidly growing Larmor-scale instabilities (namely, the firehose instability on the left side of the equation and the mirror instability on the right side) are triggered and act to regulate the pressure anisotropy back to within its stability boundaries. The lack of finite-Larmor-radius effects in the Braginskii-MHD equations means that the fastest-growing firehose modes occur at arbitrarily small scales and that the mirror mode, an inherently kinetic instability, is not described properly. How these microscale instabilities regulate the pressure anisotropy and, in doing so, place constraints on the allowed transport of momentum and heat remains very much an open question, one that has received increased attention in recent years in both the astrophysical (e.g. Schekochihin & Cowley 2006; Sharma et al. 2006) and solar wind (e.g. Gary et al. 2001; Bale et al. 2009) communities. While it is perhaps premature to judge whether the qualitative evolution found by our Braginskii-MHD description of large-scale sloshing and K-H instabilities in the ICM is contingent upon formulating a rigorous description of the kinetic microphysics, we nevertheless feel obliged to speculate upon how such microphysics may impact our results.

A key finding to emerge from (collisionless) kinetic simulations of the driven firehose instability (e.g. Matteini et al. 2006; Hellinger & Trávníček 2008; Kunz et al. 2014) is that the collisionality of the plasma, supplemented by the anomalous scattering of particles off the microscale fluctuations, adjusts to maintain a marginally firehose-stable pressure anisotropy. In a weakly collisional plasma, this effectively reduces the parallel viscosity from $\sim v_{\text{th}}^2/\nu_i$ to $\sim v_A^2/S$, where S is the shear frequency of the viscous-scale motions (Kunz et al. 2014; Mogavero & Schekochihin 2014). If this behavior holds true in the ICM, the effective Reynolds number may be in fact larger than that given by Equation 18 and K-H instabilities may develop more easily. Moreover, with the pressure anisotropy microphysically pinned at the firehose stability threshold (the left inequality of Equation 19), the resulting viscous stress would effectively cancel the magnetic tension – another effect that may ease the development of K-H instabilities. The situation with the driven mirror instability is a bit less clear (see Kunz et al. 2014; Riquelme et al. 2014), in that the pressure anisotropy appears to be regulated not just by anomalous particle scattering but also by an increasing population of resonant particles becoming trapped in magnetic mirrors where the pressure is naturally less anisotropic. It is this trapped population that has been suspected of dramatically reducing the effective thermal conductivity of the ICM (Schekochihin et al. 2008), an

effect that would call into question the applicability of the simulations in Section 3.4 to real clusters.

Clearly, more work is needed not only to assess the effects of microphysical kinetic processes on the transport of heat and momentum, but to also converge on a set of well-posed MHD-like equations that can be profitably used to study the large-scale dynamics and thermodynamics of the ICM. For now, we take comfort in the fact that the cold fronts produced in our simulations are also the locations where the magnetic-field strength is very much increased, making the inequalities (Equation 19) difficult to violate.

4.4. Anisotropic Thermal Conduction and Cold Fronts

We find in this work that the inclusion of Braginskii viscosity fails to have any significant effect on the smoothing out of cold front temperature and density jumps by anisotropic thermal conduction, despite its effect to reduce the tangling of magnetic field lines along cold front surfaces by K-H instabilities. This is perhaps not surprising, given the value of the Prandtl number of the ICM:

$$\text{Pr} \equiv \frac{\nu}{\chi} = 0.5 \frac{\ln \Lambda_e}{\ln \Lambda_i} \left(\frac{2m_e}{m_i} \right)^{1/2} \simeq 0.02. \quad (20)$$

This indicates that viscous forces operate on a much longer timescale than thermal conduction. Even if heat conduction is prevented from occurring directly across the cold front interface by a magnetic draping layer, the heating of the cold side of the front still occurs, since the front is still surrounded on multiple sides in three dimensions by hot gas that it is not magnetically isolated from (cf. Z13).

4.5. Comparison With Previous Work

We have already noted the many points of comparison between our work and that of Roediger et al. (2013a). In the limit that the magnetic field is very weak, modeling the ICM using hydrodynamics with a suppressed Spitzer viscosity would be a sufficient approximation to an MHD simulation with Braginskii viscosity to reproduce the cold fronts as we see them in observations. If the magnetic field is strong and stretched along the cold front surfaces, it will provide an additional source of suppression of K-H instabilities. Without an independent measurement of the magnetic field strength and direction, it would be difficult to determine which mechanism is largely responsible for determining the shape of the fronts. We investigate this matter further in Section 4.6.

The unmagnetized, reduced Spitzer viscosity approach is also limited when it comes to turbulence, since an isotropic viscosity will damp all modes of a turbulent cascade, whereas Braginskii viscosity will damp the magnetosonic modes only. In the sloshing cluster core, the dominant motions are solenoidal, and the resulting turbulent cascade is mainly Alfvénic. In a major merger, with strong compressible turbulence, the turbulent cascade is likely to be dominated by magnetosonic waves. The details of the effect of the different prescriptions for viscosity on this latter scenario are not straightforward to determine from the conclusions of this study, and requires further work. Though in our study the viscous dissipation scale was very small in the cluster core, in a

major merger with low densities and high temperatures this scale could be much larger, and so the differences between the two approaches at this scale would be more prevalent.

Suzuki et al. (2013) simulated the effect of isotropic and anisotropic viscosity on a “bullet” of cold gas propagating through a hot, magnetized medium. For the MHD simulations presented in their work, they assumed a uniform magnetic field direction but varied its direction with respect to the cold bullet’s velocity (along the x -axis) between the different simulations. Not surprisingly, for isotropic Spitzer viscosity they find that K-H instabilities are completely suppressed. For anisotropic viscosity, the degree of suppression is highly dependent on the magnetic field direction. For magnetic field lines perpendicular to the direction of motion of the bullet, the cold bullet sweeps these lines up into a draping layer very quickly, with the velocity gradients perpendicular to the field lines. As a result, the K-H instability is only weakly suppressed. For magnetic field lines inclined at a 45° angle to the x -axis, more suppression occurs, due to the fact that the magnetic field is more aligned with the velocity gradient initially.

In this work, our initial conditions are more appropriate for conditions in a relaxed cluster core with an initially tangled magnetic field. It is difficult to compare our results with theirs directly, due to the fact that their setup is more akin to a cold front produced by a major merger (such as in the “Bullet Cluster”) than that of sloshing motions. However, our results are consonant with theirs in the sense that Braginskii viscosity results in much less suppression of K-H instabilities than does full isotropic viscosity, except in the case where there is significant alignment of the velocity gradients with the magnetic field.

4.6. Unmagnetized Simulations

ZML11 showed that shear-amplified magnetic fields can suppress K-H instabilities in ICM cold fronts, even without viscosity, although this is highly dependent upon the strength of the initial magnetic field. The magnetic field in our simulations obviously plays a similar role, although determining whether its influence dominates over that of viscosity is complicated by the nonlinear nature of the problem. To date, most simulations of cold-front formation and evolution that included viscosity (e.g. ZuHone et al. 2010; Roediger et al. 2013a) had not included magnetic fields as well (Suzuki et al. 2013, is a notable exception). For completeness, we have performed unmagnetized versions of our “Virgo” and “AM06” simulations, both without viscosity and with an isotropic Spitzer viscosity reduced by $f = 0.1$. We also performed an unmagnetized simulation of the “AM06” model with an isotropic Spitzer viscosity reduced by $f = 0.2$. Sample temperature slices of these runs at different epochs, compared to their magnetized counterparts, are shown in Figures 14 and 15.

In the unmagnetized, inviscid simulations, more small-scale perturbations of the cold-front surface develop than in any of our magnetized simulations, since there is no mechanism (aside from the comparatively small numerical viscosity) to suppress them. More coherent large-scale instabilities are able to grow as well, which are evident in the temperature slices.

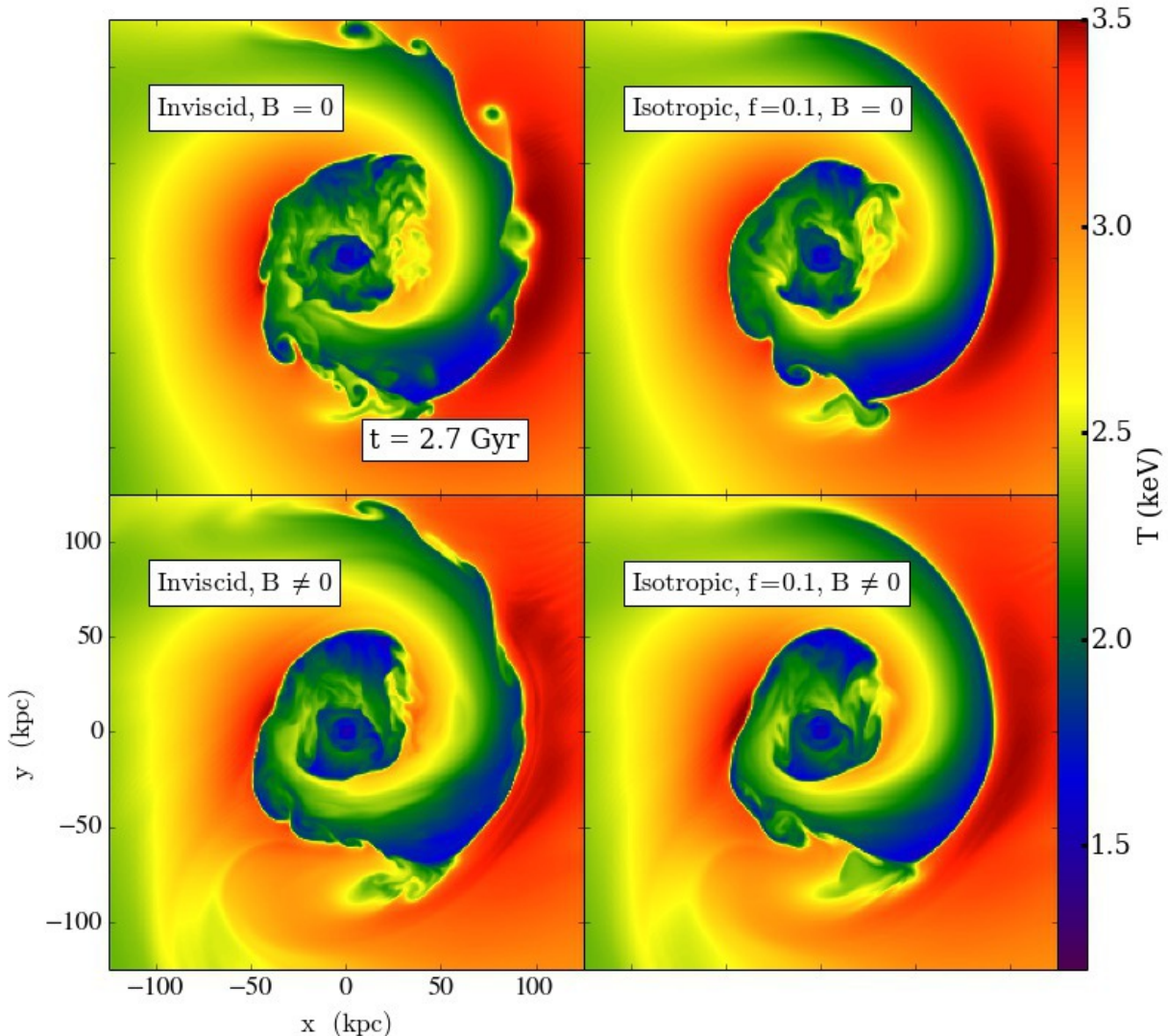


FIG. 14.— Temperature slices in keV of the unmagnetized “Virgo” simulations at the epoch $t = 2.7$ Gyr, compared to the corresponding magnetized simulations.

In the unmagnetized simulations with $f = 0.1$ Spitzer isotropic viscosity, K-H instabilities are somewhat inhibited (especially the smallest-scale perturbations), but some large-scale features still persist. In the “Virgo” simulation (Fig. 14), the cold fronts appear qualitatively similar to those in its magnetized $f = 0.1$ counterpart. This is not the case, however, in the “AM06” simulation (Fig. 15), as its cold fronts appear more disrupted by K-H instabilities than its magnetized $f = 0.1$ counterpart. This is especially true at later epochs, on length scales of several tens of kpc. The additional “AM06” unmagnetized run with $f = 0.2$ shows better qualitative agreement with the magnetized $f = 0.1$ run. This demonstrates that even the somewhat weak initial field in these simulations ($\beta \sim 1000 - 1500$, c.f. ZML11) can have a non-negligible effect on the appearance of the cold fronts, even in a viscous ICM.

These differences illustrate the difficulty in discerning the precise mechanism for K-H suppression at cold front surfaces from X-ray observations. In general, some com-

bination of the effects of viscosity and amplified magnetic fields are responsible, but these do not combine in a linear way and the separation of these two effects is complicated by the fact that, while the thermal properties of the ICM plasma are well-constrained in the vicinity of a cold front, the local magnetic-field strength is generally unknown (unless it can be constrained by other observations, e.g. radio mini-halo emission, Faraday rotation, or discontinuities in the thermal pressure—for the latter see Reiss & Keshet 2012). Unfortunately, these results indicate that there is not a general answer at this time as to whether the magnetic field or the viscosity is dominant in producing the observed smoothness of many cold fronts.

5. SUMMARY

We have performed a suite of exploratory MHD simulations of gas sloshing in a galaxy cluster core using various prescriptions for viscosity, with the aim of determining to what degree physically plausible models for

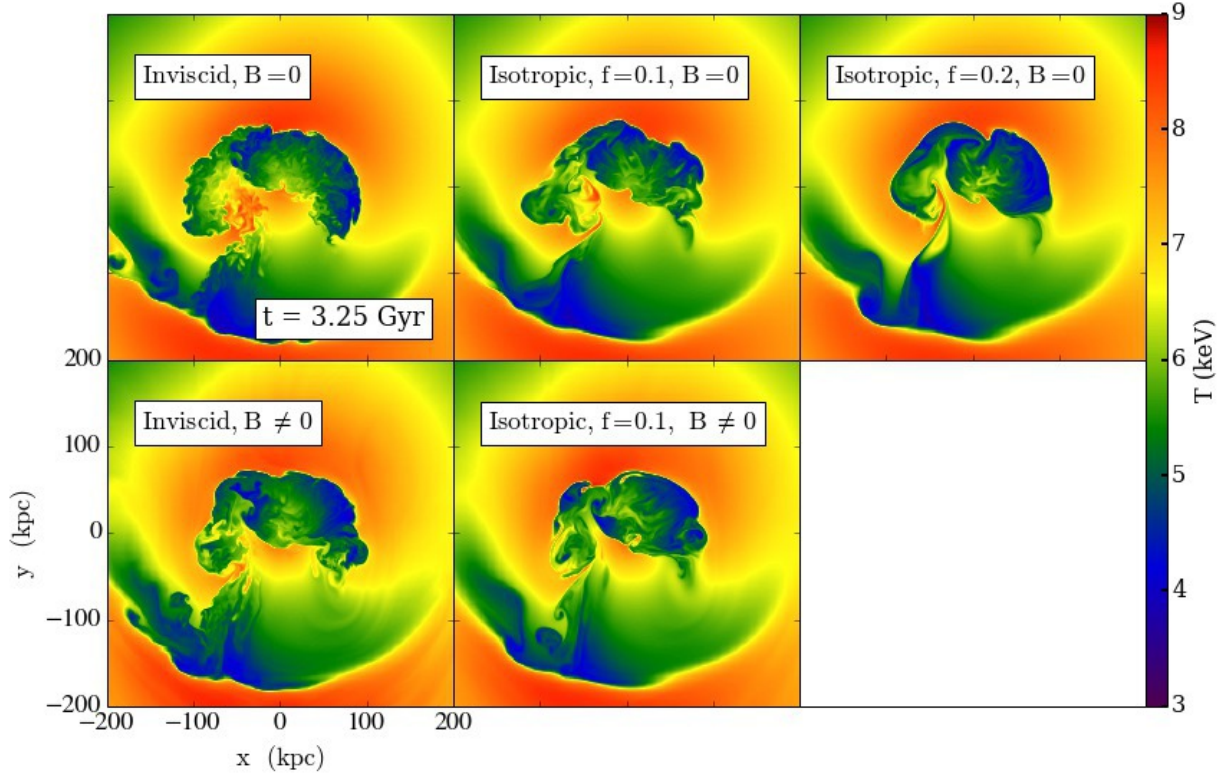


FIG. 15.— Temperature slices in keV of the unmagnetized “AM06” simulations at the epoch $t = 3.25$ Gyr, compared to the corresponding magnetized simulations.

viscosity are capable of suppressing K-H instabilities at cold fronts. We also performed simulations including viscosity and anisotropic thermal conduction to determine the joint effect of these two microphysical processes on sloshing cold fronts. Our main results are:

- We find that anisotropic Braginskii viscosity partially suppresses K-H instabilities at the surfaces of cold fronts and results in smoother fronts. However, it appears to be far less effective than isotropic viscosity, since the magnetic-field lines are oriented predominantly along the front surfaces (and therefore perpendicular to the velocity gradients).
- The suppression of turbulent motions by a full isotropic Spitzer viscosity is too extreme to be consistent with current observational indications of K-H instabilities and turbulence in galaxy cluster cores. While a more quantitative comparison with real clusters is needed (and will be presented in future work), we have found that either Braginskii viscosity or a suppressed isotropic Spitzer viscosity is needed to at least qualitatively reproduce the appearance of X-ray clusters.
- Though magnetized Braginskii viscosity is a more accurate model for the physics of the ICM, a suppressed isotropic Spitzer viscosity may provide a good qualitative approximation in terms of suppressing K-H instabilities at cold fronts. However, this conclusion depends on the magnetic-field strength and direction in the cold front region.

- The generation of cluster turbulence from sloshing motions is only somewhat inhibited by Braginskii viscosity, whereas it is completely inhibited by unsuppressed isotropic Spitzer viscosity.
- With or without Braginskii viscosity, and in cluster cores at different temperatures, an unsuppressed Spitzer conductivity along the field lines smooths out density and temperature jumps at the cold fronts to such a degree that they are inconsistent with observations.
- Unmagnetized simulations with viscosity may or may not give results that are similar to their magnetized counterparts, due to the nonlinear way in which the two effects combine to suppress K-H instabilities.

There are several directions for further research in this area. Cold fronts produced by major mergers, such as the bullet in the “Bullet Cluster” have different characteristics than sloshing cold fronts (e.g. the fact that the location of the amplified magnetic field is on the hotter side of the front rather than the colder side). Our results cannot be straightforwardly extended to this scenario, and so simulations of this kind including the same physics are needed. Other ICM features, such as AGN bubbles and cold filaments, may provide complementary constraints on the ICM viscosity. As the Braginskii-MHD equations are ill-posed at small scales and an adequate closure has yet to be developed, the study of microscale plasma instabilities and their effects on the macroscales may require

changes to our model for magnetized viscosity. The effects of resistivity (and possibly magnetic reconnection) on gas sloshing and cold fronts, particularly at the locations of amplified magnetic fields, have yet to be investigated. Finally, direct comparisons between high-exposure observations of cold fronts in real clusters and synthetic observations of simulated clusters designed to mimic these systems would further strengthen our understanding of diffusive processes in the ICM.

JAZ thanks Ian Parrish, Ralph Kraft, and Paul Nulsen for useful discussions. Calculations were performed using the computational resources of the Advanced Su-

percomputing Division at NASA/Ames Research Center. Analysis of the simulation data was carried out using the AMR analysis and visualization toolset *yt* (Turk et al. 2011), which is available for download at <http://yt-project.org>. Support for JAZ was provided by NASA through Astrophysics Theory Program Award Number 12-ATP12-0159. Support for MWK was provided by NASA through Einstein Postdoctoral Fellowship Award Number PF1-120084, issued by the *Chandra* X-ray Observatory Center, which is operated by the Smithsonian Astrophysical Observatory for and on behalf of NASA under contract NAS8-03060.

REFERENCES

- Alexiades V., Amiez G., & Gremaud P. 1996, *Commun. Num. Meth. Eng.*, 12, 31
- Asai, N., Fukuda, N., & Matsumoto, R. 2004, *ApJ*, 606, L105
- Asai, N., Fukuda, N., & Matsumoto, R. 2007, *ApJ*, 663, 816
- Ascasibar, Y., & Markevitch, M. 2006, *ApJ*, 650, 102
- Bale, S. D., Kasper J. C., Howes, G. G., Quataert E., Salem C., & Sundkvist D. 2009, *Physical Review Letters*, 103, 211101
- Biffi, V., Dolag, K., Böhringer, H., & Lemson, G. 2012, *MNRAS*, 420, 3545
- Biffi, V., Dolag, K., Böhringer, H. 2013, *MNRAS*, 428, 1395
- Bonafede, A., Feretti, L., Murgia, M., et al. 2010, *A&A*, 513, A30
- Braginskii, S. I. 1965, *Reviews of Plasma Physics*, 1, 205
- Carilli, C. L., & Taylor, G. B. 2002, *ARA&A*, 40, 319
- Chandrasekhar, S. 1961, *International Series of Monographs on Physics*, Oxford: Clarendon, 1961,
- Chew, G. F., Goldberger, M. L., & Low, F. E. 1956, *Royal Society of London Proceedings Series A*, 236, 112
- Churazov, E., Forman, W., Jones, C., Böhringer, H. 2003, *ApJ*, 590, 225
- Colella, P., & Woodward, P. R. 1984, *Journal of Computational Physics*, 54, 174
- Cowie, L. L., & McKee, C. F. 1977, *ApJ*, 211, 135
- Dong, R., & Stone, J. M. 2009, *ApJ*, 704, 1309
- Dursi, L. J. 2007, *ApJ*, 670, 221
- Dursi, L. J., & Pfrommer, C. 2008, *ApJ*, 677, 993
- Fabian, A. C., Sanders, J. S., Crawford, C. S., et al. 2003, *MNRAS*, 344, L48
- Ferrari, C., Govoni, F., Schindler, S., Bykov, A. M., & Rephaeli, Y. 2008, *Space Sci. Rev.*, 134, 93
- Gardiner, T. A., & Stone, J. M. 2005, *Journal of Computational Physics*, 205, 509
- Gardiner, T. A., & Stone, J. M. 2008, *Journal of Computational Physics*, 227, 4123
- Gary, S. P., Skoug, R. M., Steinberg, J. T., & Smith, C. W. 2001, *Geophysical Research Letters*, 33, L09101
- Ghizzardi, S., Rossetti, M., & Molendi, S. 2010, *A&A*, 516, A32
- Hellinger, P., & Trávníček, J. 2008, *Journal of Geophysical Research*, 113, A10109
- Inogamov, N. A., & Sunyaev, R. A. 2003, *Astronomy Letters*, 29, 791
- Johnson, R. E., Markevitch, M., Wegner, G. A., Jones, C., & Forman, W. R. 2010, *ApJ*, 710, 1776
- Keshet, U., Markevitch, M., Birnboim, Y., & Loeb, A. 2010, *ApJ*, 719, L74
- Kunz, M. W., Schekochihin, A. A., Cowley, S. C., Binney, J. J., & Sanders, J. S. 2011, *MNRAS*, 410, 2446
- Kunz, M. W., Bogdanović, T., Reynolds, C. S., & Stone, J. M. 2012, *ApJ*, 754, 122
- Kunz, M. W., Schekochihin, A. A., & Stone, J. M. 2014, *Physical Review Letters*, in press (arXiv:1402.0010)
- Landau, L. D., & Lifshitz, E. M. 1960, *Electrodynamics of Continuous Media* (New York: Pergamon)
- Lytikov, M. 2006, *MNRAS*, 373, 73
- Lytikov, M. 2006, *ApJ*, 668, 1
- Machacek, M., Dosaj, A., Forman, W., et al. 2005, *ApJ*, 621, 663
- Markevitch, M., Ponman, T. J., Nulsen, P. E. J., et al. 2000, *ApJ*, 541, 542
- Markevitch, M., Vikhlinin, A., & Mazzotta, P. 2001, *ApJ*, 562, L153
- Markevitch, M., Gonzalez, A. H., David, L., et al. 2002, *ApJ*, 567, L27
- Markevitch, M., Vikhlinin, A., & Forman, W. R. 2003, *Astronomical Society of the Pacific Conference Series*, 301, 37
- Markevitch, M., & Vikhlinin, A. 2007, *Phys. Rep.*, 443, 1
- Matteini, L., Landi, S., Hellinger, P., & Velli, M. 2006, *Journal of Geophysical Research*, 111, A10101
- Mazzotta, P., Markevitch, M., Vikhlinin, A., Forman, W. R., David, L. P., & VanSpeybroeck, L. 2001, *ApJ*, 555, 205
- Mogavero, F., & Schekochihin, A. A. 2014, *MNRAS*, 440, 3226
- Nulsen, P. E. J., & McNamara, B. R. 2013, *Astronomische Nachrichten*, 334, 386
- Parrish, I. J., McCourt, M., Quataert, E., & Sharma, P. 2012, *MNRAS*, 422, 704
- Reiss, I., & Keshet, U. 2012, arXiv:1208.0006
- Riquelme, M., Quataert, E., & Verscharen, D. 2014 (arXiv:1402.0014)
- Roediger, E., Brüggén, M., Simionescu, A., et al. 2011, *MNRAS*, 413, 2057
- Roediger, E., & Zuhone, J. A. 2012, *MNRAS*, 419, 1338
- Roediger, E., Kraft, R. P., Machacek, M. E., et al. 2012, *ApJ*, 754, 147
- Roediger, E., Lovisari, L., Dupke, R., et al. 2012, *MNRAS*, 420, 3632
- Roediger, E., Kraft, R. P., Forman, W. R., et al. 2013, *ApJ*, 764, 60
- Roediger, E., Kraft, R. P., Nulsen, P., et al. 2013, *MNRAS*, 436, 1721
- Ruszkowski, M., Enßlin, T. A., Brüggén, M., Heinz, S., & Pfrommer, C. 2007, *MNRAS*, 378, 662
- Ruszkowski, M., Enßlin, T. A., Brüggén, M., Begelman, M. C., & Churazov, E. 2008, *MNRAS*, 383, 1359
- Ruszkowski, M., & Oh, S. P. 2010, *ApJ*, 713, 1332
- Sarazin, C. L. 1988, *Cambridge Astrophysics Series*, Cambridge: Cambridge University Press, 1988,
- Schekochihin, A. A., Cowley, S. C., Kulsrud, R. M., Hammett, G. W., & Sharma, P. 2005, *ApJ*, 629, 139
- Schekochihin, A. A., & Cowley, S. C. 2006, *Physics of Plasmas*, 13, 056501
- Schekochihin, A. A., Cowley, S. C., Kulsrud, R. M., Rosin, M. S., & Heinemann, T. 2008, *Physical Review Letters*, 100, 081301
- Sharma, P., & Hammett, G. W. 2007, *Journal of Computational Physics*, 227, 123
- Sharma, P., Hammett, G. W., Quataert, E., & Stone J. M. 2006, *ApJ*, 637, 952
- Smith, R. K., Brickhouse, N. S., Liedahl, D. A., & Raymond, J. C. 2001, *ApJ*, 556, L91
- Spitzer, L. 1962, *Physics of Fully Ionized Gases*, New York: Interscience (2nd edition), 1962
- Srinivasan, R., & Mohr, J. J. 2001, *Bulletin of the American Astronomical Society*, 33, #100.14
- Stone, J. M., Gardiner, T. A., Teuben, P., Hawley, J. F., & Simon, J. B. 2008, *ApJS*, 178, 137
- Sunyaev, R. A., Norman, M. L., & Bryan, G. L. 2003, *Astronomy Letters*, 29, 783
- Suzuki, K., Ogawa, T., Matsumoto, Y., & Matsumoto, R. 2013, *ApJ*, 768, 175
- Turk, M. J., Smith, B. D., Oishi, J. S., Skory, S., Skillman, S. W., Abel, T., & Norman, M. L. 2011, *ApJS*, 192, 9
- Vazza, F., Roediger, E., & Brüggén, M. 2012, *A&A*, 544, A103
- Vikhlinin, A., Markevitch, M., & Murray, S. S. 2001, *ApJ*, 549, L47
- Vikhlinin, A., Markevitch, M., & Murray, S. S. 2001, *ApJ*, 551, 160
- Vikhlinin, A. A., & Markevitch, M. L. 2002, *Astronomy Letters*, 28, 495
- Zuhone, J. A., Markevitch, M., & Johnson, R. E. 2010, *ApJ*, 717, 908 (ZMJ10)
- Zuhone, J. A., Markevitch, M., & Lee, D. 2011, *ApJ*, 743, 16 (ZML11)
- Zuhone, J. A., Markevitch, M., Ruszkowski, M., & Lee, D. 2013, *ApJ*, 762, 69 (Z13)
- Zuhone, J. A., Markevitch, M., Brunetti, G., & Giacintucci, S. 2013, *ApJ*, 762, 78

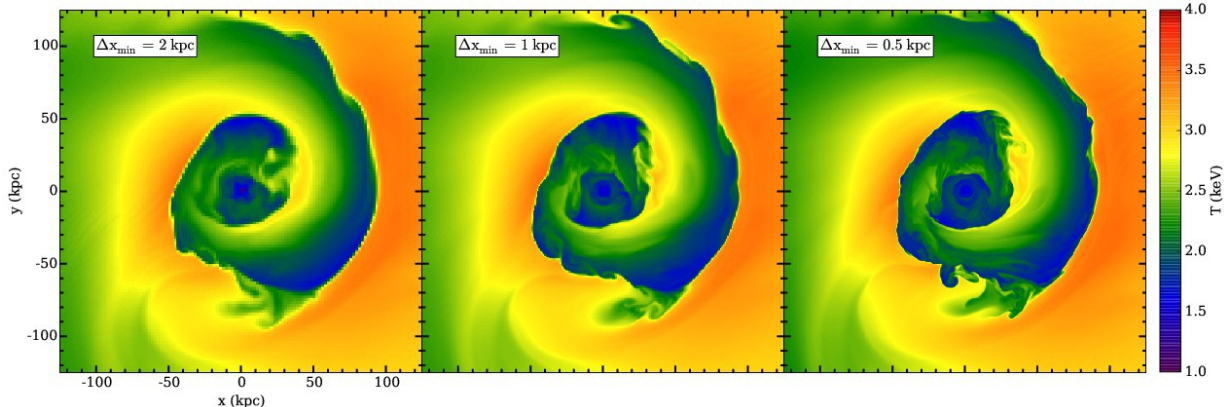


FIG. B16.— Slices of temperature through the center of the simulation domain for inviscid “Virgo” simulations with varying resolution at time $t = 2.7$ Gyr.

APPENDIX

A. RESOLUTION TEST

We found in ZML11 that the ability of the magnetic field to suppress K-H instabilities was somewhat resolution-dependent. To test the dependence of our results on spatial resolution, we performed simulations of our “Virgo” model at a finest resolution of $\Delta x = 2$ kpc and $\Delta x = 0.5$ kpc, bracketing our default resolution of $\Delta x = 1$ kpc. Figure B16 shows slices of temperature through the center of the simulation domain at time $t = 2.7$ Gyr. Though the increase in resolution permits more small-scale instabilities to develop, the overall behavior on larger scales (structures of \sim tens of kpc) is the same. Since these are the scales that X-ray telescopes will be able to observe, we conclude that our default resolution of $\Delta x = 1$ kpc is more than adequate for the purposes of this paper.

B. SYNTHETIC X-RAY OBSERVATIONS

Our synthetic X-ray observations have been generated by a module derived from the PHOX code (Biffi et al. 2012, 2013) that has been specifically designed for use with yt (Turk et al. 2011). In the first step, we determine each cell’s specific photon emissivity using an APEC (Smith et al. 2001) model from its density and temperature and assumed metallicity. Using this emissivity as a distribution function for the photon energies, we generate photon samples from each cell assuming an exposure time of $t_{\text{exp}} = 300$ ks and collecting area $A_{\text{coll}} = 6000$ cm². This ensures that we have a large number of photon samples. In the second step, the photons are projected along a given line of sight, and the energies are shifted by the line-of-sight velocity and the cosmological redshift. A subset of the photons are chosen by adjusting the exposure time, accounting for Galactic absorption via a `thabs` model, and assuming an energy-dependent effective area. For the latter we use the on-axis effective area curve of the ACIS-S3 chip on *Chandra*. Since we are not performing spectral analysis, we have not applied any spectral responses. The simulated events are then binned into an image with pixels that correspond to the same size as the finest SMR cells in the simulation ($\Delta x \approx 1$ kpc). Details on the yt X-ray observation module may be found at http://yt-project.org/doc/analyzing/analysis_modules/photon_simulator.html.